nature chemistry

Article

https://doi.org/10.1038/s41557-023-01287-x

Enhanced active-site electric field accelerates enzyme catalysis

Received: 13 March 2023

Accepted: 29 June 2023

Published online: 10 August 2023

Check for updates

Chu Zheng [1,3], Zhe Ji [1,3], Irimpan I. Mathews[2] & Steven G. Boxer [1]

The design and improvement of enzymes based on physical principles remain challenging. Here we demonstrate that the principle of electrostatic catalysis can be leveraged to substantially improve a natural enzyme's activity. We enhanced the active-site electric field in horse liver alcohol dehydrogenase by replacing the serine hydrogen-bond donor with threonine and replacing the catalytic Zn^{2+} with Co^{2+}. Based on the electric field enhancement, we make a quantitative prediction of rate acceleration—50-fold faster than the wild-type enzyme—which was in close agreement with experimental measurements. The effects of the hydrogen bonding and metal coordination, two distinct chemical forces, are described by a unified physical quantity—electric field, which is quantitative, and shown here to be additive and predictive. These results suggest a new design paradigm for both biological and non-biological catalysts.

Enzymes are extraordinarily proficient and selective catalysts arising from billions of years of evolution[1,2]. Because of their astonishing catalytic proficiency, the rational design of proteins that outperform enzymes, especially in their native functions, remains a grand challenge. Current de novo designed enzymes[3–5] generally exhibit relatively poor activities. This can be improved by directed evolution[5–8]; however, this is not grounded in an underlying physical principle. A growing amount of evidence shows that the large electric fields created by charged and polar enzyme active sites contribute substantially to enzyme catalysis[9–12]. This principle of electrostatic catalysis, however, has largely been demonstrated by making the electric fields and catalytic rates smaller, leaving open the possibility to make faster enzymes and catalysts based on stronger electrostatics. In this work, we report enhancements in electric fields in the active site of horse liver alcohol dehydrogenase (LADH), probed using the vibrational Stark effect, by mutagenesis and active-site metal exchange. We found that these enhanced electric fields accelerate the rates of hydride transfer, an effect that is quantitatively predicted, additive in double mutants and applicable beyond the scope of naturally occurring enzymes.

LADH catalyses a reversible reaction, either the oxidation of alcohol into aldehydes/ketones by NAD^+ or the reduction of aldehydes/ketones into alcohols by NADH[13]. In the reductive pathway (Fig. 1a), LADH, cofactor NADH and an aldehyde/ketone substrate form a ternary complex, where the carbonyl (C=O) in the substrate interacts strongly with a catalytic Zn^{2+} and an hydrogen-bond donor, S48. The C=O is subject to a nucleophilic attack by the hydride from NADH, proceeding to a transition state with an elongation of the C=O bond and more charge separation along the bond axis. As a result, the C=O in the transition state bears a larger dipole ($\boldsymbol{\mu}_{TS}$) than that in the reactant state ($\boldsymbol{\mu}_{RS}$) (Fig. 1b). An enzyme electric field ($\mathbf{F}_{enz}$), created by the elements of the active site, in this case primarily Zn^{2+} and hydrogen-bonded S48, interacts with the change in C=O dipole ($\boldsymbol{\mu}_{TS} - \boldsymbol{\mu}_{RS}$), and could accelerate the hydride transfer reaction by lowering the free-energy barrier according to $\Delta\Delta G^{\ddagger} = -\mathbf{F}_{enz} \cdot (\boldsymbol{\mu}_{TS} - \boldsymbol{\mu}_{RS})$ (Fig. 1c). The transition state then turns into an oxyanion intermediate before forming the alcohol product (Fig. 1a). Under this framework, we expected that enhancing active-site electric fields could accelerate enzyme catalysis. Although a study of an artificial enzyme based on electric field calculations[14] supports our hypothesis, experimental measurement of the electric field enhancement is missing, which is especially challenging and important for naturally occurring enzymes. In previous studies[11,15], mutations of active-site residues invariably reduce the measured electric field, slow down the reactions (smaller rate constant k_{cat}) and increase the free-energy barrier ($\Delta G^{\ddagger}$). Here we ask whether the field can be made larger and whether $\Delta G^{\ddagger}$ decreases correspondingly (Fig. 1c). This is an ultimate experimental test of the principle of electrostatic catalysis and its application in designing functional enzymes and catalysts in general.

[1]Department of Chemistry, Stanford University, Stanford, CA, USA. [2]Stanford Synchrotron Radiation Lightsource, Menlo Park, CA, USA. [3]These authors contributed equally: Chu Zheng, Zhe Ji. e-mail: sboxer@stanford.edu

https://doi.org/10.1038/s41557-023-01287-x

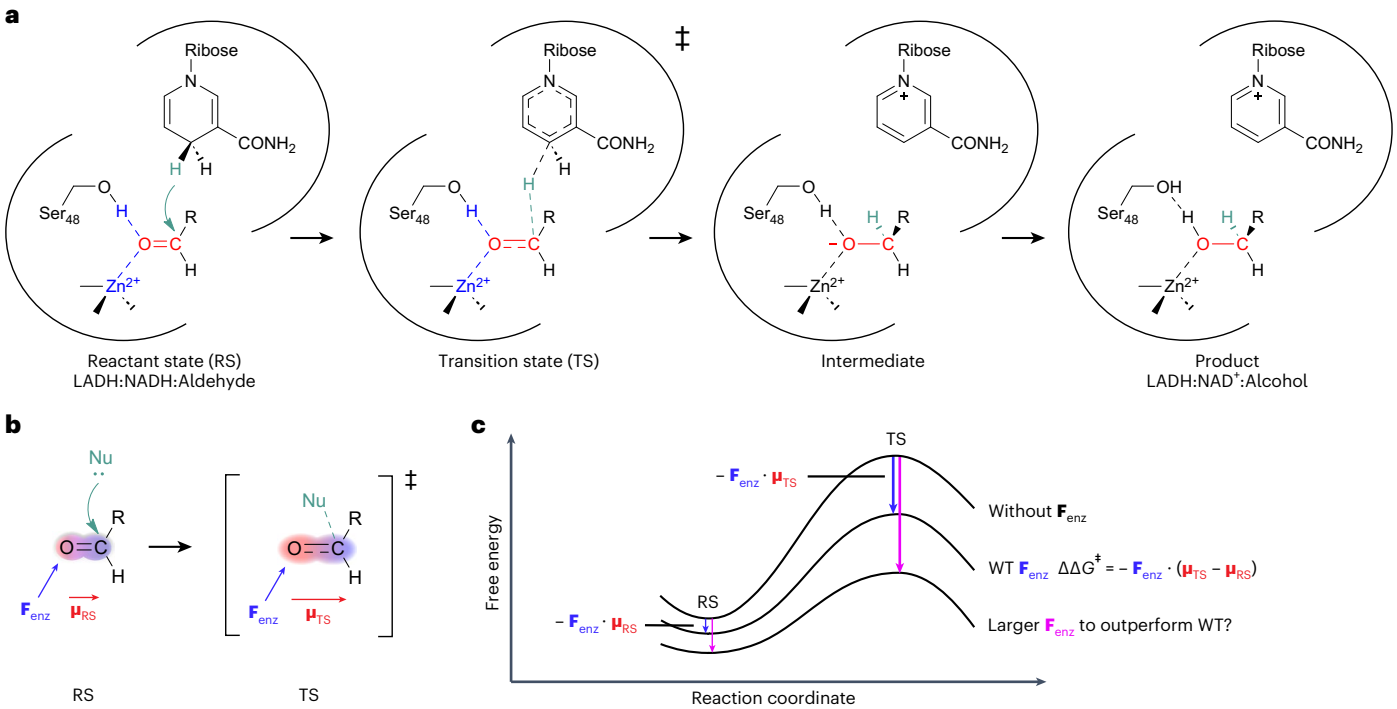

Fig. 1 | Electrostatic catalysis of LADH. a, Mechanism of aldehyde hydrogenation catalysed by LADH using NADH as the cofactor. **b**, An aldehyde forms the transition state upon a nucleophilic attack. The enzyme active site exerts an electric field ($\mathbf{F}_{enz}$) on the carbonyl bond (C=O) dipole, which increases from the reactant state ($\boldsymbol{\mu}_{RS}$) to the more charge-separated transition state ($\boldsymbol{\mu}_{TS}$). **c**, The active site electric field $\mathbf{F}_{enz}$ lowers the activation barrier by $\Delta\Delta G^{\ddagger}$ through preferential stabilization of $\boldsymbol{\mu}_{TS}$ over $\boldsymbol{\mu}_{RS}$. Note that the fields are exerted by the charges and dipoles organized by the protein structure itself, not to be confused with an externally applied field[44–48]. WT, wild-type.

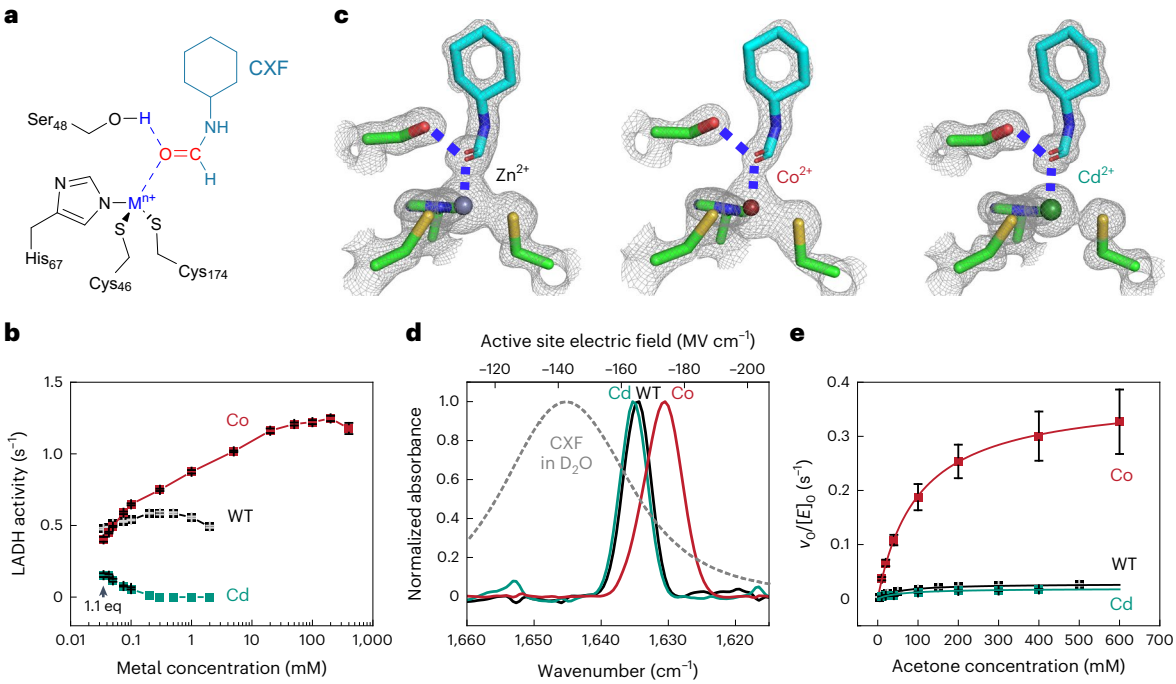

Fig. 2 | Metal exchange in the active site of LADH. a, Schematic active site of LADH bound to CXF. NADH is omitted for simplicity. **b**, LADH activity in ethanol dehydrogenation after incubating apo-LADH with the metal ions overnight at 4 °C. Data are presented as mean values ± s.d. based on $n = 3$ independent replicates. See Supplementary Methods. **c**, Crystal structures of wild-type LADH at 1.43 Å resolution (PDB 7RM6), LADH^{Co} at 1.65 Å resolution (PDB 8EIW), and LADH^{Cd} at 1.33 Å resolution (PDB 7UTW). The nitrogen atoms are denoted by the colour blue, oxygen by red, sulfur by yellow, carbon atoms from the protein by green, carbon atoms from the inhibitor (CXF) by cyan, Zn by grey, Co by darker red and Cd by darker green. **d**, Infrared spectra of the C=O in CXF bound to the active site of wild-type LADH, LADH^{Co} and LADH^{Cd}. The top electric field axis is mapped from the bottom frequency axis according to: $\bar{\nu} = 0.47F + 1712.2$ (Supplementary Fig. 2), where $\bar{\nu}$ is the wavenumber (cm^{-1}) of the C=O vibrations and F is the magnitude of the electric fields (MV cm^{-1}) projected on the C=O. **e**, Michaelis–Menten kinetics of acetone hydrogenation by wild-type LADH, LADH^{Co} and LADH^{Cd}. $[E]_0$ was determined by the number of active-site metal ions as quantified by inductively coupled plasma atomic emission spectroscopy. Data are presented as mean values ± s.d. based on $n = 3$ independent replicates. See Supplementary Methods for more details.

https://doi.org/10.1038/s41557-023-01287-x

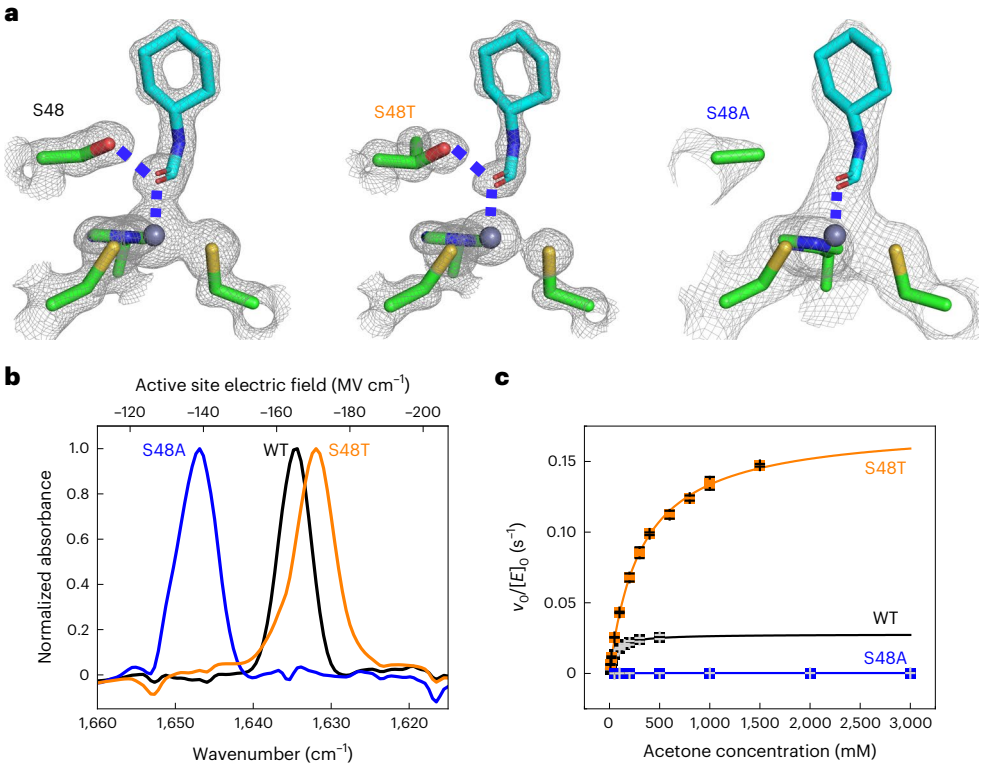

Fig. 3 | Hydrogen-bond perturbation in the active site of LADH. a, Crystal structures of wild-type LADH at 1.43 Å resolution (PDB 7RM6), LADH^{S48T} at 1.40 Å resolution (PDB 7UQ9) and LADH^{S48A} at 2.20 Å resolution (PDB 7U9N), each bound to the inhibitor CXF. See Fig. 2a for the schematic structure. **b**, Infrared spectra of the C=O in CXF bound to the active site of wild-type LADH, LADH^{S48T} and LADH^{S48A}. See Fig. 2d caption for details. **c**, Michaelis–Menten kinetics of acetone hydrogenation by wild-type LADH, LADH^{S48T} and LADH^{S48A}. See Fig. 2e caption for details.

Results

Changing active-site electric field by metal replacement

As shown in Fig. 2a, the catalytic Zn^{2+} in the LADH active site adopts a tetrahedral coordination geometry comprised of residues of H67, C46 and C174, with the fourth ligand being the C=O of either a substrate or, in the current work, an inhibitor, *N*-cyclohexylformamide (CXF)[16–18]. To modify the electric field exerted by the metal ion, we replaced the active-site Zn^{2+} with other metal ions[19–22], including Cd^{2+} and Co^{2+}, by developing a new metal removal–insertion method (Supplementary Methods, Supplementary Fig. 1 and Supplementary Tables 1 and 2). The metal insertion was optimized by systematically varying the metal ion concentrations and measuring alcohol dehydrogenation activity (Fig. 2b). We obtained the crystal structures of wild-type LADH, LADH^{Co} and LADH^{Cd} (Fig. 2c and Supplementary Table 3). The three structures overlap well, including the coordination geometry of the metal ions, the positioning of NADH and the length of the hydrogen bond between S48 and the CXF C=O. Zn^{2+} and Co^{2+} are both about 2.2 Å away from the oxygen of the CXF C=O; for Cd^{2+}, this distance is slightly longer at 2.4 Å as expected given the ionic radius. All the metal–O–C angles are ~110°.

To measure the electric fields in the active site of LADH, we employed CXF (Fig. 2a), a substrate-analogue inhibitor whose C=O stretching vibration can probe the local electrostatic interactions imposed on the aldehyde/ketone substrates by the LADH active site. The calibration of the C=O vibrational probe (Supplementary Methods, Supplementary Fig. 2 and Supplementary Tables 4 and 5) enables us to utilize the vibrational Stark effect to translate the measured C=O vibrational frequencies into the absolute magnitudes of the electric fields projected onto the C=O bond. Using isotope-edited infrared spectroscopy (Supplementary Methods), we unambiguously identified the C=O vibrational peaks of CXF bound to the wild-type and mutants of LADH (note that we refer to the metal-exchanged proteins also as mutants for simplicity) (Fig. 2d, Supplementary Fig. 3 and Supplementary Table 6). In the wild-type LADH, the C=O frequency of CXF is 1,634.6 cm^{-1}, mapping to F_{enz} = −165 MV cm^{-1} (the negative sign represents a stabilizing interaction with the C=O dipole), a very large field, considerably larger than the average field projected on this bond in water (Fig. 2d). For LADH^{Co} and LADH^{Cd}, the CXF C=O was redshifted to 1,630.6 cm^{-1} and blueshifted to 1,635.2 cm^{-1}, respectively, corresponding to a larger field of −174 MV cm^{-1} in LADH^{Co} and a slightly smaller field of −164 MV cm^{-1} in LADH^{Cd}. To elucidate the connection between these electric fields and the hydride transfer in LADH, we measured the Michaelis–Menten kinetics of LADH-catalysed acetone hydrogenation (Supplementary Methods and Supplementary Table 7). Acetone was chosen as the substrate because (1) it has a rate-limiting hydride transfer reaction[23,24], so that k_{cat} can approximate the hydride transfer rate, and (2) its transition state analogue shows similar bond positioning as CXF[25], so that the electric fields probed by the carbonyl group of CXF are catalytically relevant (Supplementary Text 1 and Supplementary Fig. 4). We observed a dramatic 14-fold increase in k_{cat} of acetone hydrogenation by LADH^{Co} compared with LADH^{Zn} (Fig. 2e, Supplementary Fig. 5 and Supplementary Table 8). LADH^{Cd} showed slightly smaller k_{cat} compared with LADH^{Zn}.

Changing active-site electric field by site-directed mutation

We next perturbed the hydrogen bond of S48, another key contributor to the active site, by making the S48A and S48T mutants[26], which still bind CXF (Fig. 3a, Supplementary Tables 9 and 10, Supplementary Fig. 6 and Supplementary Text 2). The S48A mutation removed the hydrogen-bond interaction and thus markedly blueshifted the C=O band and reduced the active-site electric field projected on the C=O to −139 MV cm^{-1} (Fig. 3b, Supplementary Fig. 3 and Supplementary Table 6). By contrast, the S48T mutation redshifted the C=O frequency,

https://doi.org/10.1038/s41557-023-01287-x

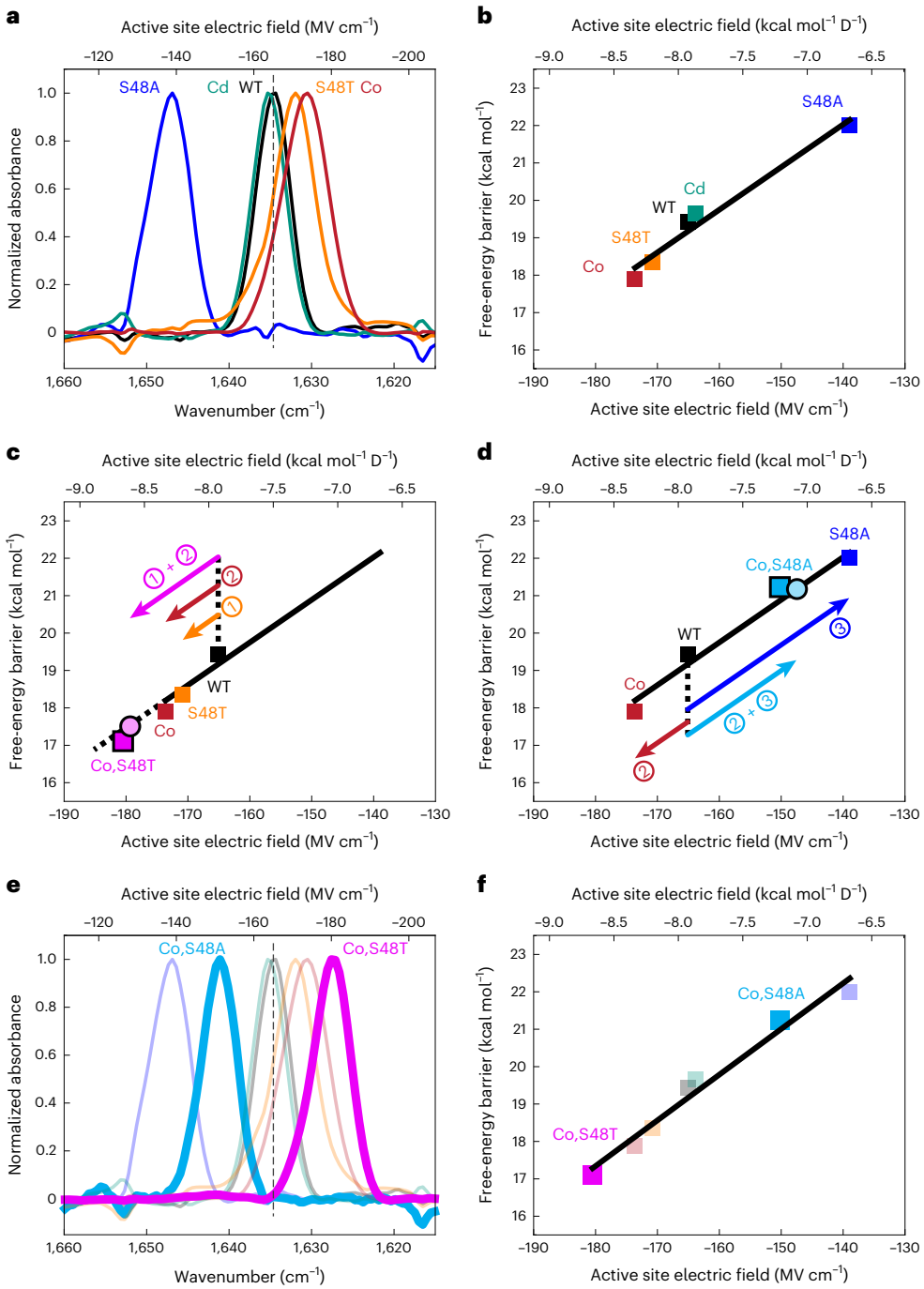

Fig. 4 | A unifying electrostatic basis for enzyme catalysis and design. **a**, Infrared spectra of the C=O in CXF bound to the active site of LADH variants. See Fig. 2d caption for details. **b**, Plot of the free-energy barrier ($\Delta G^{\ddagger}$) of acetone hydrogenation against F experienced by the CXF C=O. $\Delta G^{\ddagger}$ was calculated based on transition state theory using k_{cat} determined by kinetic studies (Supplementary Tables 8 and 11). The linear regression gave $\Delta G^{\ddagger} = 2.38F_{enz} + 38.0$ ($R^2 = 0.97$), with $\Delta G^{\ddagger}$ in kcal mol^{-1} and F in kcal mol^{-1} D^{-1}, a unit manifesting the physical meaning of the slope, which is the reaction difference dipole in debye (Supplementary Text 3). **c**, Same plot as **b** showing the prediction of the double mutant LADH^{Co,S48T} as the sum of the single mutants LADH^{S48T} (1) and LADH^{Co} (2) in terms of F_{enz} and $\Delta G^{\ddagger}$ with respect to the wild-type. The prediction (magenta circle) is in close agreement with the experimental data (magenta square). **d**, Same plot as **b** showing the prediction of the double mutant, LADH^{Co,S48A}, as the sum of the single mutants LADH^{Co} (2) and LADH^{S48A} (3) in terms of F_{enz} and $\Delta G^{\ddagger}$ with respect to the wild-type. The prediction (blue circle) is in close agreement with the experimental data (blue square). **e**, An extension of **a** including the spectra for the double mutants LADH^{Co,S48T} and LADH^{Co,S48A}. **f**, An extension of **b** by adding the data for the double mutants LADH^{Co,S48T} and LADH^{Co,S48A}. The updated linear regression gave $\Delta G^{\ddagger} = 2.54F_{enz} + 39.3$ ($R^2 = 0.97$).

leading to a larger field than the wild-type of −171 MV cm^{-1}. The S48A mutation dramatically decreases the k_{cat} of acetone hydrogenation by 80-fold compared with the wild-type, while LADH^{S48T} shows a k_{cat} that is 6.3-fold larger than that of the wild-type (Fig. 3c, Supplementary Fig. 5 and Supplementary Table 8). Although the S48A mutation directly removes the hydrogen bond, the metal exchange and the S48T mutation did not produce notable structural changes for the bound C=O, as observed from crystallography (Figs. 2c and 3a). Nonetheless, their

electrostatic effects can be sensitively reported from direct readouts of vibrational spectroscopy.

Quantitative predictions of enzyme activity

As shown in Fig. 4a,b, the free-energy barrier ($\Delta G^{\ddagger}$) of the reaction and the active-site electric field (Supplementary Table 11) show a linear correlation (Supplementary Text 3) over a wide range of both parameters, which indicates that the catalytic effects of the hydrogen bond and the metal ions, despite their different chemical properties, both have a common electrostatic nature and can be quantitatively described using electric fields. To test whether the electric field, a physical quantity, is additive, we set out to design double mutants that harness the sum of the effects of single mutants. Specifically, we designed LADH^{Co,S48T} and LADH^{Co,S48A}, and made quantitative predictions for both their fields and activities (Fig. 4c,d). Given that Co^{2+} and S48T mutations enhance the electric fields by −8.5 MV cm^{-1} and −5.7 MV cm^{-1}, respectively, if the fields are additive, we predicted that LADH^{Co,S48T} would improve the field by −14.2 MV cm^{-1} compared with the wild-type, reaching −179.4 MV cm^{-1}, which would lead to $\Delta G^{\ddagger}$ = 17.5 kcal mol^{-1} based on the linear correlation (Fig. 4c). These predictions were found to be in close agreement with the experimental results (F_{enz} = −180.5 MV cm^{-1} and $\Delta G^{\ddagger}$ = 17.1 kcal mol^{-1}; Supplementary Fig. 7), resulting in a variant that substantially surpasses the wild-type in the rate of hydride transfer: 52-fold for acetone hydrogenation. The other double mutant, LADH^{Co,S48A}, combines a field-diminishing S48A with a field-enhancing Co^{2+} replacement, which therefore was predicted to rescue the deleterious effect of S48A (Fig. 4d). Indeed, the decrease in electric field (+26.2 MV cm^{-1}) due to S48A relative to wild-type is partially offset by the increase in electric field (−8.5 MV cm^{-1}) due to Co^{2+}, resulting in a total field change of +17.7 MV cm^{-1}. The predicted F_{enz} = −147.4 MV cm^{-1} and $\Delta G^{\ddagger}$ = 21.2 kcal mol^{-1} again match well with the experimental results (F_{enz} = −150.2 MV cm^{-1} and $\Delta G^{\ddagger}$ = 21.2 kcal mol^{-1}; Supplementary Fig. 7). These positive and negative designs clearly demonstrate the additivity of electric fields and a precise electrostatic control of enzyme activities that can both outperform a natural enzyme and fill a continuous activity spectrum (Fig. 4e,f).

Discussion

Previous studies have used vibrational frequency shifts to infer how enzymes work. Substrate binding was found to be favoured in enzyme active sites based on the redshift of the CXF C=O in LADH[16]. Rate enhancement due to enzyme electrostatic environment was evidenced by redshift of the pyruvate C=O in lactate dehydrogenase[27], but was interpreted to be a consequence of bond polarization. Instead of bond polarization, our previous work[11,12,15,28] used the vibrational Stark effect to interpret vibrational frequency shifts, showing a linear correlation between the free-energy barrier and the active-site electric field, a physics-based quantity. The results summarized in Fig. 4f are striking as now the linear correlation extends both to slower rates and smaller fields than wild-type, but also to larger rates and fields. This suggests a general strategy that has been largely absent[14,29–33] in the enzyme design community: a focus on the electric field created by the elements of the active site. These same concepts apply to chemical reactivity in general, whether for biological or non-biological reactions in organized environments.

The results show that the hydride transfer reaction of horse LADH can be improved by only a single mutation, changing serine to threonine, or by replacing the catalytic Zn^{2+} with Co^{2+}. Threonine is found at the same site in yeast[34] and human liver[35] alcohol dehydrogenase; however, Co^{2+} unlocks a design space unavailable to nature. Unlike the native incorporation of Zn^{2+} from its micromolar environment in vivo, the insertion of Co^{2+} was facilitated by incubating the apo-LADH with millimolar Co^{2+} (Fig. 2b), so LADH^{Co} is not expected in nature. The best variant, LADH^{Co,S48T}, also outperforms the wild-type in carrying out the reverse alcohol dehydrogenation reaction; ethanol, the natural substrate, is transformed 2.4-fold faster (Supplementary Table 12). This reverse reaction has also been studied within the framework of electrostatic catalysis, although its mechanism is more complicated than the hydride transfer step (Supplementary Text 4 and Supplementary Fig. 8), and our carbonyl probe relates most directly to the hydride transfer step.

The language of electric fields has been used to describe a variety of molecular interactions[36,37], including hydrogen bonds, halogen bonds, dipole–dipole interactions and induced dipole interactions, but to date not coordinate bonds where metal is the electric field producer. Our results show that the metal–carbonyl coordination in the active site of LADH, where the metal is Zn^{2+}, Cd^{2+} or Co^{2+} and the carbonyl is a part of an aldehyde or ketone (Fig. 1a), can also be treated within this framework. This simple, classical picture allows us to analyse local interactions that are less accessible from theories such as ligand field theory[38], which addresses the global symmetry and properties of coordination complexes. The electric field is also a different language from Lewis acidity as the strength of Lewis acidity is a relative quantity[39], often entangled with that of Lewis basicity of the Lewis adduct partner[40]. In contrast, the electric field explicitly describes the energetic effect of a metal ion on a ligand bond dipole on an absolute scale and with physics-based units. Most importantly, whereas concepts such as Lewis acidity are validated by thermodynamics (free-energy changes and equilibrium constants), the active-site electric field can address functionally relevant kinetics because it directly affects both the bond dipoles of the reactant and transition states (Fig. 1b,c).

The ability of our electrostatic model to capture the faster-than-wild-type reactions in LADH^{Co}, LADH^{S48T} and LADH^{Co,S48T} reinforces the importance and universality of electrostatic catalysis as a basic physical principle applicable beyond the scope of naturally occurring enzymes and as a useful design principle for directed evolution and protein engineering. Given the power of electric fields to describe molecular interactions in a local and absolute manner, and the additive[41] and quantitative nature of these fields, together with the rapid developments of de novo protein design programmes[3–5,42,43] and computational tools[14,29–33], we envision a promising future within reach to fully harness the power of electrostatic catalysis to design faster enzymes than those produced naturally, and to create chemical catalysts with wide applications.

Online content

Any methods, additional references, Nature Portfolio reporting summaries, source data, extended data, supplementary information, acknowledgements, peer review information; details of author contributions and competing interests; and statements of data and code availability are available at https://doi.org/10.1038/s41557-023-01287-x.

References

1. Radzicka, A. & Wolfenden, R. A proficient enzyme. *Science* **267**, 90–93 (1995).
2. Risso, V. A., Gavira, J. A., Mejia-Carmona, D. F., Gaucher, E. A. & Sanchez-Ruiz, J. M. Hyperstability and substrate promiscuity in laboratory resurrections of precambrian β-lactamases. *J. Am. Chem. Soc.* **135**, 10580–10580 (2013).
3. Huang, P. S., Boyken, S. E. & Baker, D. The coming of age of de novo protein design. *Nature* **537**, 320–327 (2016).
4. Lovelock, S. L. et al. The road to fully programmable protein catalysis. *Nature* **606**, 49–58 (2022).
5. Kries, H., Blomberg, R. & Hilvert, D. De novo enzymes by computational design. *Curr. Opin. Chem. Biol.* **17**, 221–228 (2013).
6. Arnold, F. H. & Volkov, A. A. Directed evolution of biocatalysts. *Curr. Opin. Chem. Biol.* **3**, 54–59 (1999).
7. Bunzel, H. A. et al. Evolution of dynamical networks enhances catalysis in a designer enzyme. *Nat. Chem.* **13**, 1017–1022 (2021).

8. Otten, R. et al. How directed evolution reshapes the energy landscape in an enzyme to boost catalysis. *Science* **370**, 1442–1446 (2020).
9. Villa, J. & Warshel, A. Energetics and dynamics of enzymatic reactions. *J. Phys. Chem. B* **105**, 7887–7907 (2001).
10. Warshel, A. et al. Electrostatic basis for enzyme catalysis. *Chem. Rev.* **106**, 3210–3235 (2006).
11. Fried, S. D., Bagchi, S. & Boxer, S. G. Extreme electric fields power catalysis in the active site of ketosteroid isomerase. *Science* **346**, 1510–1514 (2014).
12. Fried, S. D. & Boxer, S. G. Electric fields and enzyme catalysis. *Annu. Rev. Biochem.* **86**, 387–415 (2017).
13. Plapp, B. V. et al. Horse liver alcohol dehydrogenase: zinc coordination and catalysis. *Biochemistry* **56**, 3632–3646 (2017).
14. Vaissier, V., Sharma, S. C., Schaettle, K., Zhang, T. R. & Head-Gordon, T. Computational optimization of electric fields for improving catalysis of a designed kemp eliminase. *ACS Catal.* **8**, 219–227 (2018).
15. Schneider, S. H. & Boxer, S. G. Vibrational Stark effects of carbonyl probes applied to reinterpret IR and Raman data for enzyme inhibitors in terms of electric fields at the active site. *J. Phys. Chem. B* **120**, 9672–9684 (2016).
16. Deng, H., Schindler, J. F., Berst, K. B., Plapp, B. V. & Callender, R. A Raman spectroscopic characterization of bonding in the complex of horse liver alcohol dehydrogenase with NADH and *N*-cyclohexylformamide. *Biochemistry* **37**, 14267–14278 (1998).
17. Ramaswamy, S., Scholze, M. & Plapp, B. V. Binding of formamides to liver alcohol dehydrogenase. *Biochemistry* **36**, 3522–3527 (1997).
18. Zheng, C. et al. A two-directional vibrational probe reveals different electric field orientations in solution and an enzyme active site. *Nat. Chem.* **14**, 891–897 (2022).
19. Dietrich, H., Maret, W., Wallen, L. & Zeppezauer, M. Active-site-specific reconstituted cobalt(II) horse-liver alcohol dehydrogenase: changes of the spectra of the substrate *trans*-4-(*N*,*N*-dimethylamino)-cinnamaldehyde and of the catalytic cobalt ion upon ternary complex formation with NADH and 1,4,5,6-tetrahydronicotinamide–adenine dinucleotide. *Eur. J. Biochem.* **100**, 267–270 (1979).
20. Schneider, G., Cedergren-Zeppezauer, E., Knight, S., Eklund, H. & Zeppezauer, M. Active site specific cadmium(II)-substituted horse liver alcohol dehydrogenase: crystal structures of the free enzyme, its binary complex with NADH, and the ternary complex with NADH and bound *p*-bromobenzyl alcohol. *Biochemistry* **24**, 7503–7510 (1985).
21. Schneider, G., Eklund, H., Cedergren-Zeppezauer, E. & Zeppezauer, M. Crystal structures of the active site in specifically metal-depleted and cobalt-substituted horse liver alcohol dehydrogenase derivatives. *Proc. Natl Acad. Sci. USA.* **80**, 5289–5293 (1983).
22. Schneider, G., Eklund, H., Cedergren-Zeppezauer, E. & Zeppezauer, M. Structure of the complex of active site metal-depleted horse liver alcohol dehydrogenase and NADH. *EMBO J.* **2**, 685–689 (1983).
23. Adolph, H. W., Kiefer, M. & Zeppezauer, M. in *Enzymology and Molecular Biology of Carbonyl Metabolism 4* (eds Weiner, H. et al.) 401–410 (Springer, 1993).
24. Adolph, H. W., Maurer, P., Schneider-Bernlohr, H., Sartorius, C. & Zeppezauer, M. Substrate specificity and stereoselectivity of horse liver alcohol dehydrogenase. Kinetic evaluation of binding and activation parameters controlling the catalytic cycles of unbranched, acyclic secondary alcohols and ketones as substrates of the native and active-site-specific Co(II)-substituted enzyme. *Eur. J. Biochem.* **201**, 615–625 (1991).
25. Al-Karadaghi, S. et al. Refined crystal structure of liver alcohol dehydrogenase-NADH complex at 1.8 Å resolution. *Acta Crystallogr. D* **50**, 793–807 (1994).
26. Kim, K. & Plapp, B. V. Inversion of substrate stereoselectivity of horse liver alcohol dehydrogenase by substitutions of Ser-48 and Phe-93. *Chem. Biol. Interact.* **276**, 77–87 (2017).
27. Deng, H. et al. Source of catalysis in the lactate dehydrogenase system. Ground-state interactions in the enzyme–substrate complex. *Biochemistry* **33**, 2297–2305 (1994).
28. Schneider, S. H., Kratochvil, H. T., Zanni, M. T. & Boxer, S. G. Solvent-independent anharmonicity for carbonyl oscillators. *J. Phys. Chem. B* **121**, 2331–2338 (2017).
29. Fuxreiter, M. & Warshel, A. Origin of the catalytic power of acetylcholinesterase: computer simulation studies. *J. Am. Chem. Soc.* **120**, 183–194 (1998).
30. Roca, M., Vardi-Kilshtain, A. & Warshel, A. Toward accurate screening in computer-aided enzyme design. *Biochemistry* **48**, 3046–3056 (2009).
31. Vaissier Welborn, V. & Head-Gordon, T. Computational design of synthetic enzymes. *Chem. Rev.* **119**, 6613–6630 (2019).
32. Welborn, V. V., Ruiz Pestana, L. & Head-Gordon, T. Computational optimization of electric fields for better catalysis design. *Nat. Catal.* **1**, 649–655 (2018).
33. Hennefarth, M. R. & Alexandrova, A. N. Direct look at the electric field in ketosteroid isomerase and its variants. *ACS Catal.* **10**, 9915–9924 (2020).
34. Raj, S. B., Ramaswamy, S. & Plapp, B. V. Yeast alcohol dehydrogenase structure and catalysis. *Biochemistry* **53**, 5791–5803 (2014).
35. Niederhut, M. S., Gibbons, B. J., Perez-Miller, S. & Hurley, T. D. Three-dimensional structures of the three human class I alcohol dehydrogenases. *Protein Sci.* **10**, 697–706 (2001).
36. Fried, S. D. & Boxer, S. G. Measuring electric fields and noncovalent interactions using the vibrational Stark effect. *Acc. Chem. Res.* **48**, 998–1006 (2015).
37. Vaissier Welborn, V., Archer, W. R. & Schulz, M. D. Characterizing ion–polymer interactions in aqueous environment with electric fields. *J. Chem. Inf. Model.* **63**, 2030–2036 (2023).
38. Griffith, J. S. & Orgel, L. E. Ligand-field theory. *Q. Rev.* **11**, 381–393 (1957).
39. Anslyn, E. V. & Dougherty, D. A. *Modern Physical Organic Chemistry* (University Science, 2006).
40. Drago, R. S., Vogel, G. C. & Needham, T. E. 4-parameter equation for predicting enthalpies of adduct formation. *J. Am. Chem. Soc.* **93**, 6014–6026 (1971).
41. Lin, C. Y., Romei, M. G., Mathews, I. I. & Boxer, S. G. Energetic basis and design of enzyme function demonstrated using GFP, an excited-state enzyme. *J. Am. Chem. Soc.* **144**, 3968–3978 (2022).
42. Anishchenko, I. et al. De novo protein design by deep network hallucination. *Nature* **600**, 547–552 (2021).
43. Wang, J. et al. Scaffolding protein functional sites using deep learning. *Science* **377**, 387–394 (2022).
44. Shaik, S. S. & Stuyver, T. *Effects of Electric Fields on Structure and Reactivity: New Horizons in Chemistry* (Royal Society of Chemistry, 2021).
45. Shaik, S., Danovich, D., Joy, J., Wang, Z. & Stuyver, T. Electric-field mediated chemistry: uncovering and exploiting the potential of (oriented) electric fields to exert chemical catalysis and reaction control. *J. Am. Chem. Soc.* **142**, 12551–12562 (2020).
46. Shaik, S., Mandal, D. & Ramanan, R. Oriented electric fields as future smart reagents in chemistry. *Nat. Chem.* **8**, 1091–1098 (2016).
47. Aragones, A. C. et al. Electrostatic catalysis of a diels-alder reaction. *Nature* **531**, 88–91 (2016).
48. Zang, Y. P. et al. Directing isomerization reactions of cumulenes with electric fields. *Nat. Commun.* **10**, 4482 (2019).

Reporting summary

Further information on research design is available in the Nature Portfolio Reporting Summary linked to this article.

Data availability

The X-ray coordinates and structural factors of LADH variants complexed with NADH and CXF have been deposited in the Protein Data Bank (PDB) as entries 7UQ9 ($LADH^{S48T}$), 8EIW ($LADH^{Co}$), 7UTW ($LADH^{Cd}$), 7U9N ($LADH^{S48A}$), 8EIY ($LADH^{Co,S48T}$) and 8EIX ($LADH^{Co,S48A}$). The structure 2OHX was also used in this study and is accessible in the PDB. All the data that support the finding of this study are available within this article, Supplementary Information and provided source data.

Acknowledgements

We thank B. V. Plapp at the University of Iowa for providing detailed guidance on the expression and purification of LADH and much other valuable advice. We thank I. Andersson at Uppsala University and W. Maret at King's College London for their advice on the metal substitution of LADH. We thank A. Braun, A. Heyer and M. Brueggemeyer for the data analysis and discussion of $LADH^{Co}$; G. Li at the Stanford Environmental Measurements Facility (EMF) for the inductively coupled plasma atomic emission spectroscopy data collection; T. McLaughlin from Stanford University Mass Spectrometry (SUMS) for the measurements of native mass spectrometry; T. Carver at the Stanford Nano Shared Facilities (SNSF) for nickel coating Stark windows. C.Z. is grateful for a Stanford Center for Molecular Analysis and Design (CMAD) Fellowship. This work was supported by NIH grant GM118044 (to S.G.B.). Use of the Stanford Synchrotron Radiation Lightsource, SLAC National Accelerator Laboratory, is supported by the US Department of Energy, Office of Science, Office of Basic Energy Sciences under contract number DE-AC02-76SF00515. The SSRL Structural Molecular Biology Program is supported by the DOE Office of Biological and Environmental Research, and by the National Institutes of Health, National Institute of General Medical Sciences (P30GM133894). The contents of this publication are solely the responsibility of the authors and do not necessarily represent the official views of NIGMS or NIH. The funders had no role in study design, data collection and analysis, decision to publish or preparation of the paper.

Author contributions

C.Z. and S.G.B. designed the research. C.Z. and Z.J. performed most of the experiments and data analysis, including expression and purification of LADH variants, metal substitution of LADH, infrared spectroscopy and enzyme kinetic studies. C.Z. and I.I.M. performed X-ray crystallography and solved the crystal structures of LADH variants. C.Z., Z.J. and S.G.B discussed the results and wrote the paper.

Competing interests

The authors declare no competing interests.

Additional information

Supplementary information The online version contains supplementary material available at https://doi.org/10.1038/s41557-023-01287-x.

Correspondence and requests for materials should be addressed to Steven G. Boxer.

Peer review information *Nature Chemistry* thanks the anonymous reviewers for their contribution to the peer review of this work.

nature portfolio

Corresponding author(s): Steven G. Boxer

Last updated by author(s): Jun 15, 2023

Reporting Summary

Nature Portfolio wishes to improve the reproducibility of the work that we publish. This form provides structure for consistency and transparency in reporting. For further information on Nature Portfolio policies, see our Editorial Policies and the Editorial Policy Checklist.

Statistics

For all statistical analyses, confirm that the following items are present in the figure legend, table legend, main text, or Methods section.

n/a	Confirmed	
☐	☒	The exact sample size (*n*) for each experimental group/condition, given as a discrete number and unit of measurement
☐	☒	A statement on whether measurements were taken from distinct samples or whether the same sample was measured repeatedly
☒	☐	The statistical test(s) used AND whether they are one- or two-sided *Only common tests should be described solely by name; describe more complex techniques in the Methods section.*
☒	☐	A description of all covariates tested
☒	☐	A description of any assumptions or corrections, such as tests of normality and adjustment for multiple comparisons
☐	☒	A full description of the statistical parameters including central tendency (e.g. means) or other basic estimates (e.g. regression coefficient) AND variation (e.g. standard deviation) or associated estimates of uncertainty (e.g. confidence intervals)
☒	☐	For null hypothesis testing, the test statistic (e.g. *F*, *t*, *r*) with confidence intervals, effect sizes, degrees of freedom and *P* value noted *Give P values as exact values whenever suitable.*
☒	☐	For Bayesian analysis, information on the choice of priors and Markov chain Monte Carlo settings
☒	☐	For hierarchical and complex designs, identification of the appropriate level for tests and full reporting of outcomes
☒	☐	Estimates of effect sizes (e.g. Cohen's *d*, Pearson's *r*), indicating how they were calculated

Our web collection on statistics for biologists contains articles on many of the points above.

Software and code

Policy information about availability of computer code

Data collection	The IR data were collected on a Bruker Vertex 70 spectrometer using OPUS 5.0. The kinetic data were collected using PerkinElmer UV WinLab 6.4.0.973. The x-ray crystallographic data were collected by Blu-Ice 5.0 at SSRL.
Data analysis	The IR data were analyzed by OPUS 5.0. The kinetic data were analyzed using Igor Pro 8.04. The x-ray crystallographic data were analyzed by Phenix 1.18.2-3874 and COOT 0.8.9.2.

For manuscripts utilizing custom algorithms or software that are central to the research but not yet described in published literature, software must be made available to editors and reviewers. We strongly encourage code deposition in a community repository (e.g. GitHub). See the Nature Portfolio guidelines for submitting code & software for further information.

Data

Policy information about availability of data

All manuscripts must include a data availability statement. This statement should provide the following information, where applicable:

- Accession codes, unique identifiers, or web links for publicly available datasets
- A description of any restrictions on data availability
- For clinical datasets or third party data, please ensure that the statement adheres to our policy

The x-ray coordinates and structural factors of LADH variants complexed with NADH and CXF have been deposited in the Protein Data Bank (PDB) as entries 7UQ9

(LADHS48T), 8EIW (LADHCo), 7UTW (LADHCd), 7U9N (LADHS48A), 8EIY (LADHCo,S48T), and 8EIX (LADHCo,S48A). The structure 2OHX was also used in this study and accessible from PDB. All the data that support the finding of this study are available within this article and its Supplementary Information.

Human research participants

Policy information about studies involving human research participants and Sex and Gender in Research.

Reporting on sex and gender	N/A
Population characteristics	N/A
Recruitment	N/A
Ethics oversight	N/A

Note that full information on the approval of the study protocol must also be provided in the manuscript.

Field-specific reporting

Please select the one below that is the best fit for your research. If you are not sure, read the appropriate sections before making your selection.

☒ Life sciences ☐ Behavioural & social sciences ☐ Ecological, evolutionary & environmental sciences

For a reference copy of the document with all sections, see nature.com/documents/nr-reporting-summary-flat.pdf

Life sciences study design

All studies must disclose on these points even when the disclosure is negative.

Sample size	A sample size of 22,027 - 150,245 reflections were used for x-ray structural refinements. 7 - 14 kinetic samples with different substrate concentrations were used for enzyme kinetic measurements. A sample size of nine different solvents were used for solvatochromism studies to determine the linear field-frequency correlation. A sample size of seven different enzyme variants were used to determine the linear correlation between the active site electric field and free energy barrier.
Data exclusions	No data were excluded from the analyses.
Replication	Three independent replicates were performed and successfully reproduced the results of this work.
Randomization	A subset of 5% of reflections (1106 - 7516) were randomly selected by Phenix for calculating Rfree and were not used in refinement. Randomization was not performed for IR and kinetics experiments and is not applicable for those studies.
Blinding	Blinding was not performed for IR, kinetics, and x-ray crystallography experiments and is not applicable for those studies.

Reporting for specific materials, systems and methods

We require information from authors about some types of materials, experimental systems and methods used in many studies. Here, indicate whether each material, system or method listed is relevant to your study. If you are not sure if a list item applies to your research, read the appropriate section before selecting a response.

Materials & experimental systems

n/a	Involved in the study
☒	☐ Antibodies
☒	☐ Eukaryotic cell lines
☒	☐ Palaeontology and archaeology
☒	☐ Animals and other organisms
☒	☐ Clinical data
☒	☐ Dual use research of concern

Methods

n/a	Involved in the study
☒	☐ ChIP-seq
☒	☐ Flow cytometry
☒	☐ MRI-based neuroimaging

nature chemistry

Article

https://doi.org/10.1038/s41557-023-01287-x

Enhanced active-site electric field accelerates enzyme catalysis

In the format provided by the authors and unedited

Table of Contents

Materials and Methods

Chemicals are from the following sources, without further purification: *N*-cyclohexylformamide (CXF, Sigma-Aldrich, 99%), hexane (Sigma-Aldrich, 99%), toluene (Sigma-Aldrich, 99.8%), dibutyl ether (Sigma-Aldrich, 99%), chloroform (Sigma-Aldrich, 99.8%), tetrahydrofuran (Sigma-Aldrich, 99.8%), dichloromethane (Sigma-Aldrich, 99.8%), acetonitrile (Sigma-Aldrich, 99.8%), dimethyl formamide (Sigma-Aldrich, 99.8%), dimethyl sulfoxide (Sigma-Aldrich, 99.8%), cyclohexylamine (99%), sodium formate-^{13}C (99% atom % ^{13}C), glycer(ol-D_3) (Sigma-Aldrich, 99 atom % D), deuterium oxide (ACROS, 100.0 atom % D), acetone (Sigma-Aldrich, 99.8%), 2-propanol (Sigma-Aldrich, 99.9%), NAD^+ (Roche, Grade I, free acid), NADH (Roche, Grade I, disodium salt), sodium pyrophosphate decahydrate (Sigma-Aldrich, 99%), cobalt(II) acetate (Sigma-Aldrich, 99.99% trace metals basis), cadmium(II) acetate (Sigma-Aldrich, anhydrous 99.995%), 2,6-pyridinedicarboxylic acid (Sigma-Aldrich, 99%), TES and its sodium salt (Sigma-Aldrich, 99%), Chelex 100 chelating resin (Biorad, molecular biology grade, 200-400 mesh, catalog No. 1421253), cobalt standard for ICP (Sigma-Aldrich), cadmium standard for ICP (Sigma-Aldrich), zinc standard for ICP (Sigma-Aldrich), tert-butanol (Sigma-Aldrich, 99.7%). N-[formyl-^{13}C]-cyclohexylformamide (^{13}C-CXF) was synthesized as previously reported.[1]

1. Plasmid construction and protein sequence

As reported previously,[1,2] the gene sequence of wild-type liver alcohol dehydrogenase (LADH) was inserted into a recombinant DNA expression plasmid (pET-15b, Genscript Inc.) along with a strep tag and a cleavage site for *Tobacco etch virus* (TEV) protease. Point mutations were

made using the QuikChange Lightning Site-Directed Mutagenesis Toolkit (Agilent). The gene and protein sequences are shown below.

1.1 Gene sequence

atggcgagctggtctcatccgcagtttgaaaaaggcgcggaaaatctgtattttcagggcgcgggtagcacagcaggaaaagtaataaaat
gcaaagcggctgtgctgtgggaggaaaagaaaccattttccatcgaggaggtggaggttgcacccccgaaggcccatgaagtccgtataa
agatggtggccacaggaatttgtcgctcagatgaccacgtggttagtggaacccttgtcacacctcttcctgtgatcgcaggccatgaggcag
cgggcattgtggagagcattggagaaggcgtcactacagtaagaccaggtgataaagtcatcccactctttactccccagtgtggaaaatgc
agggtttgtaagcaccctgaaggcaacttctgcttgaaaaatgatctgagcatgcctcggggaaccatgcaggatggtaccagcaggttcac
ctgcagagggaagcccatccaccacttccttggcaccagcaccttctcccagtacaccgtggtggacgagatctcagtggccaagatcgatg
cggcctcaccgctggagaaagtctgtctcattggctgtggattttctactggttatgggtctgcagtcaaggttgccaaggtcacccagggctc
cacctgtgccgtgtttggccttggaggagtgggcctgtctgttatcatgggctgtaaagcagccggagcggccaggatcattggggtggacat
caacaaagacaagtttgcaaaggccaaagaagtgggtgccactgagtgtgtcaaccctcaggactacaagaaacccatccaggaggtgct
gacagaaatgagcaatggaggtgtggatttttcctttgaagtcattggtcggctcgacactatggtgactgccttgtcatgctgtcaagaagc
atatggtgtgagcgtcattgtgggagtacctcctgattcccaaaatctctctatgaatcctatgttgctactgagtggacgtacctggaaagga
gctatttttggcggttttaagagtaaagattctgtccccaaacttgtggccgattttatggctaaaaagtttgcactggatcctttaatcaccca
tgttttacctttgaaaaaataaatgaaggatttgacctgcttcgctctggagagagtatccgtaccatcctgacgttttga

1.2 Protein sequence of LADH with a strep tag (GREEN) and TEV cleavage site (YELLOW)[a]

MASWSHPQFEKGAENLYFQ|GAGSTAGKVIKCKAAVLWEEKKPFSIEEVEVAPPKAHEVRIKMVATGICRSDD
HVVSGTLVTPLPVIAGHEAAGIVESIGEGVTTVRPGDKVIPLFTPQCGKCRVCKHPEGNFCLKNDLSMPRGTMQ
DGTSRFTCRGKPIHHFLGTSTFSQYTVVDEISVAKIDAASPLEKVCLIGCGFSTGYGSAVKVAKVTQGSTCAVFGL
GGVGLSVIMGCKAAGAARIIGVDINKDKFAKAKEVGATECVNPQDYKKPIQEVLTEMSNGGVDFSFEVIGRLDT
MVTALSCCQEAYGVSVIVGVPPDSQNLSMNPMLLLSGRTWKGAIFGGFKSKDSVPKLVADFMAKKFALDPLIT
HVLPFEKINEGFDLLRSGESIRTILTF

[a] "|" indicates the cleavage position.

2. Protein expression and purification

As previously described,[1] wildtype LADH and its variants were expressed using the *Escherichia coli* cell line [BL21(DE3), New England BioLabs Inc.] in Lysogeny broth (LB) medium (Miller) in the presence of ampicillin (0.1 g/L). After an overnight (16-18 hours) growth at 23 °C, cell pellets were collected by centrifugation at 6800 ×g (fixed angle, 6000 rpm) for 30 minutes at 4 °C and then resuspended in 100 mM Tris-HCl buffer at pH 8.0 containing 150 mM NaCl and 10%

(v/v) glycerol. Cells were lysed using a mechanical homogenizer (Avestin EmulsiFlex-C3), and the lysates were centrifuged at 26700 ×g (fixed angle, 15000 rpm) for 90 minutes at 4 °C. The resultant supernatants were further filtered (0.22 μm) and then loaded onto the strep column (StrepTrap HP, Catalog No. 28907547, GE Healthcare). After the strep-tag purification, the protein was treated with TEV protease (Gene and Cell Technologies Inc.) to cleave the strep tag for 16 hours at 4 °C. The tag-free protein was then purified by anion exchange column (HiTrap Q HP, Catalog No. 17115401, GE Healthcare) at pH 9.5 (20 mM piperazine). The identity and purity of protein were characterized by electrospray ionization mass spectrometry (Waters 2795 HPLC with ZQ single quadrupole MS in Stanford University Mass Spectrometry facility).

3. Metal replacement of the catalytic Zn^{2+} of LADH

Although the metal replacement of the catalytic Zn^{2+} in LADH has been reported using microcrystals of LADH and dialysis to remove the catalytic Zn^{2+},[3,4] this method has several practical drawbacks: (1) the dialysis process is slow and consumes a substantial amount of solvents; (2) it is inconvenient to monitor the enzyme activity during the process as one needs to open the dialysis bag, take out protein crystals, and redissolve crystals into the buffer for measuring kinetics (this process also usually leads to a significant loss of protein samples because it is difficult to control the amount of protein crystals taken out for activity measurements); (3) the frequent operations of opening and closing dialysis bags increase the risk of sample leakage especially given that LADH is colorless. We therefore sought to develop a new preparation method that could circumvent those issues by directly doing metal exchange in the solution instead of with microcrystals.

To avoid any possible metal contamination during this process, we removed any trace metal ions in the buffer by treating it with a suspension of Chelex 100 chelating resin of at least 1 g/L in the buffer for one hour, followed by removing the resin by a 0.22 μm filter. This is necessary because some metal ions (e.g. Zn^{2+} and Cd^{2+}) have a strong binding affinity to apo LADH; even a trace metal contamination in buffers can lead to substantial undesired metalation of LADH. This metal removal procedure was also performed for buffers used in other experiments involving the metal exchange.

For the depletion of catalytic Zn^{2+}, we chose 10 mM dipicolinic acid (DPA) as the chelating agent to remove the active site Zn^{2+} as DPA was shown in previous work[3] to selectively pull out the catalytic Zn^{2+} while keeping the second, structural Zn^{2+} in place. Specifically, we prepared a buffer containing 100 mM TES sodium and 10 mM DPA and adjusted the pH to 6.9. All the following experiments were performed at 4°C but inert gas protection or reducing agents were found to be unnecessary. Wildtype LADH was buffer exchanged into the TES sodium/DPA solution using a 10 kDa MWCO Amicon spin filter (Millipore). We then performed buffer exchange using the same type of spin filter every five hours or overnight, seven times in total, to push the reaction equilibrium of Zn^{2+} depletion toward completion. Finally, we removed DPA by buffer exchanging the protein into a DPA-free 100 mM TES sodium buffer at pH 6.9. The obtained protein usually had a remaining activity of 2% of the wild type, which was comparable to the previous studies.[3] Our attempt to separate the remaining wild type enzyme from the apo enzyme by anion exchange chromatography was unsuccessful due to their similar elution time. However, we note that the remaining wildtype enzyme has negligible impact on $LADH^{Co}$ and $LADH^{Cd}$'s kinetics for acetone hydrogenation because they have similar or higher catalytic rate constants

compared with the wild type. The remaining wild type in the prepared apo enzyme was also undetectable in the protein IR measurements.

For metal ion insertion, different metal ions are expected to have different binding affinities, and some may cause enzyme denaturation at high concentrations. Therefore, to find the optimal condition for metal insertion, we incubated apo-LADH with metal ions of varying concentrations overnight and then measured the ethanol dehydrogenation activity (see the Methods section 11) of those samples. The reconstituted wildtype $LADH^{Zn}$ reached a maximal activity after incubating with 0.2-0.5 mM Zn^{2+} (Fig. 2b), while higher Zn^{2+} concentrations decreased the activity. Cd^{2+}, another Zn group element, dramatically decreased the activity once its concentration went above 0.035 mM (1.1 molar equivalent). For $LADH^{Co}$, the activity plateaued as the Co^{2+} concentration reached 200 mM, while 82% activity was obtained at 5 mM Co^{2+}, indicating an equilibrium established among the free Co^{2+}, apo-LADH, and $LADH^{Co}$.

After we found the optimal concentration for metal insertion, we scaled up this process to prepare samples for kinetic and spectroscopic experiments. Specifically, 0.033 mM apo enzyme (mg scale) was incubated overnight with 5 mM cobalt(II) acetate to prepare $LADH^{Co}$ or 0.03 mM cadmium acetate to prepare $LADH^{Cd}$. The Cd^{2+} was added at 0.9 equivalent to the apo enzyme to avoid off-target binding given the presumption that the active site is the strongest binding site for Cd^{2+}.

The obtained $LADH^{Co}$ and $LADH^{Cd}$ were characterized by inductively coupled plasma atomic emission spectroscopy (ICP-AES), crystallography, native mass spectrometry, isotope-edited FTIR spectroscopy, and enzyme kinetics (the following sections). All these experiments were performed immediately after removing the excess metal ion in the solution by buffer

exchange using either a 10 kDa MWCO Amicon spin filter (Millipore) or a Micro BioSpin P-6 gel column (Bio-Rad) (depending on the volume), except for crystallography where we maintain excess Co^{2+} in the crystallization solution for the $LADH^{Co}$ variants. When excess Co^{2+} was removed, spontaneous metal dissociation was not observed in the period of experiments evidenced by the unchanged UV-Vis spectrum of $LADH^{Co}$ and the time-independent catalytic performance.

4. Validation of Co oxidation state in $LADH^{Co}$ as +2

Because $LADH^{Co}$ displayed higher hydride transfer rates and larger electric fields, we considered the possibility that the Co may be in a higher oxidation state, e.g. Co^{3+}, producing the larger field. It is noteworthy that Co^{3+} is unlikely in this case because: (1) $LADH^{Co}$ was prepared using the air-stable salt of Co^{2+} acetate; Co^{2+} is generally thought difficult to be oxidized to Co^{3+} by O_2 in air, the mostly likely oxidant if the oxidation were to happen, given the standard redox potential (+1.92 V for Co^{3+}/Co^{2+} vs +1.23 V for O_2/H_2O); (2) the distorted tetrahedral coordination geometry we observed from the x-ray structure of $LADH^{Co}$, very similar to the wild type with Zn^{2+}, would be highly unusual for Co^{3+}; and (3) Co^{2+} is well known as a good substitute for Zn^{2+} and has been used to replace Zn^{2+} in a variety of zinc enzymes,[3,5-10] including LADH.[3,10] To further confirm the oxidation state of +2 for the cobalt in our prepared sample, we measured $LADH^{Co}$ by UV-Vis spectroscopy and observed absorption features at 648 and 354 nm, corresponding to the d-d transition of the Co^{2+} and the ligand-metal charge transfer [S(Cys) → Co^{2+} charge transfer], respectively, at the active site (Supplementary Fig. 1a), consistent with the literature,[3,10,11] which confirms an oxidation state of +2 of the active-site Co. Treating the $LADH^{Co}$ with ascorbic acid (see the next paragraph) led to a decrease in the UV-Vis absorption band of the bound Co^{2+} at 648 nm,

corresponding to the Co^{2+} d-d transition $^4A_2 \rightarrow {}^4T_1$ (P),[10] and the enzyme activity (Supplementary Fig. 1b-c), indicating a reduction of the Co^{2+} to Co^{1+}, in support of the oxidation state assignment. As shown in Supplementary Fig. 1d,e, $LADH^{Co,S48T}$ displays the same UV-Vis absorption at 354 nm and 648 nm as $LADH^{Co}$ does, indicating an unchanged Co oxidation state of +2 in $LADH^{Co,S48T}$.

In the reduction of $LADH^{Co}$ by ascorbic acid, all the buffers were treated with Chelex 100 resin as described earlier and purged under argon in conjunction with sonication to remove dissolved oxygen in the buffers as much as possible (we did not bubble the buffers with argon to avoid contamination of metal ions from the needle). $LADH^{Co}$ was buffer exchanged into the 100 mM TES buffer (pH 6.9) that contains an excess amount of ascorbic acid. For 0.028 mM $LADH^{Co}$ in 20 mM ascorbic acid or 0.28 mM $LADH^{Co}$ in 200 mM ascorbic acid, more than 88% of Co^{2+} was reduced after two hours under argon at room temperature as monitored by the decrease in the absorption at 648 nm, which corresponds to the d-d transition band of the bound Co^{2+} (Supplementary Fig. 1b). Leaving the protein at room temperature for longer than two hours led to protein denaturation as evidenced by features of scattering in UV-Vis spectra. We minimized the exposure of the samples to air because the reduced Co^{1+} can be oxidized back to Co^{2+} when the excess ascorbic acid is depleted, as evidenced by the recovery of LADH's activity for ethanol dehydrogenation (Supplementary Fig. 1c). During this process, ascorbic acid was oxidized by Co^{2+} which was in turn continuously regenerated by air. Essentially, $LADH^{Co}$ became the catalyst for the oxidation of ascorbic acid by air.

5. ICP-AES

To quantify the amount of metal ions in the LADH active sites, we lyophilized 1.5 mg of LADH (quantified based on the absorbance at 280 nm and ε(280 nm) = 18 $mM^{-1}cm^{-1}$ from the literature[12]) and digested the protein by adding 200 μL of 70% nitric acid (>99.999% trace metal basis, Sigma-Aldrich). The mixture was left at room temperature for 2 days before dilution to 7 mL using metal-free water (Milli-Q water treated by Chelex 100 chelating resin as described above). The final concentration of nitric acid was 2%. The solution was passed through a syringe filter (0.2 μM, Millipore) before measurement by inductively coupled plasma atomic emission spectroscopy (ICP-AES). Blank and standard solutions of target metals were prepared at a series of concentrations using the 1000 mg/L metal standards obtained from Sigma-Aldrich. ICP-AES was measured at Stanford Environmental Measurements Facility using a Thermo Scientific ICAP 6300 Duo View Spectrometer. The measured concentrations of metal ions were converted to the molar ratios as shown in Supplementary Table 2. The ratio of the active-site Co to the structural Zn was found to range from 0.56 to 0.87 for $LADH^{Co}$, $LADH^{Co,S48A}$, and $LADH^{Co,S48T}$. The imperfect Co insertion originates from the relatively weak binding of Co to the active site. In contrast, Cd shows 100% binding to the active site. Both metal binding affinities agree with the observation of ethanol activity measurements, where a high cobalt concentration was needed to achieve peak activities (Fig. 2b).

6. X-Ray crystallography of LADH

Conditions similar to wild type[1] were used for growing crystals of $LADH^{S48T}$, $LADH^{S48A}$, and $LADH^{Cd}$ variants, i.e., 50 mM Tris-HCl buffer at pH 7.80 containing varying amounts of PEG400 (10% - 28%) as reservoir solutions. The protein sample contained 25 mg/mL LADH, 4 mM NADH and 20 mM CXF. To set up a protein drop, 1.1 μL of protein sample was added on a plastic coverslip, followed by the addition of 1.1 μL of reservoir solution on the protein drop. Crystals were grown at 4 °C and typically harvested within a week. For $LADH^{Co}$, $LADH^{Co,S48A}$, and $LADH^{Co,S48T}$, using PEG400 as precipitant only produced tiny protein crystals that were unusable for X-ray crystallography. Therefore, we used tert-butanol for those Co^{2+}-containing LADH variants. Specifically, the reservoir solutions contained varying amounts of tert-butanol (12% - 22%) along with 2 mM cobalt(II) acetate [for $LADH^{Co}$ and $LADH^{Co,S48T}$] or 5 mM cobalt(II) acetate for $LADH^{Co,S48A}$. The protein sample contained 25 mg/mL protein with 4 mM NADH and 10 mM CXF. Other steps were similar to those for non-Co^{2+}-containing LADH variants.

To prepare samples for X-ray crystallography, a single crystal was looped and dipped into the cryoprotectant (mother liquor with 30% PEG400) before flash cooling in liquid nitrogen. X-ray diffraction data were collected at 100 K at the Stanford Synchrotron Radiation Lightsource (Menlo Park, CA) at beamline BL12-1 and BL12-2. S48A, $LADH^{Co,S48A}$ and $LADH^{Co,S48T}$ formed less high-quality crystals and gave poorer diffraction and resolution than other LADH variants. The structures were solved using the Molecular Replacement Module from PHENIX, where the initial model was a published 1.43 Å structure of wildtype LADH in complex with NADH and CXF (PDB: 7RM6). Several rounds of manual and automatic structure refinement were performed using

COOT and PHENIX to ensure the data fitting converges according to some standard metrics. The data collection and refinement statistics are shown in Supplementary Table 3.

7. Native mass spectrometry for metal replaced LADH variants

The protein samples were analyzed by LC-ESI/MS on the Agilent 1260 HPLC and Bruker MicroTOF-Q II. The column was a polyhydroxyethyl A from PolyLC operated in size exclusion mode: 200×4.6 mm, 5 μm of beads with 1000 Å of pore size, flow rate of 0.2 mL/min with 200 mM ammonium acetate isocratic. The injection volume was 15 μL, except for the quality control (QC) sample (0.5 mg/mL carbonic anhydrase), which was 5 μL. Data were collected in full scan MS mode with a mass range of 1500-8000 Da. The collision RF setting was 3000 Vpp. The results are shown in Supplementary Table 1.

8. Vibrational Stark spectroscopy

As previously described,[1] CXF was dissolved in a mixture of D_2O and glycer(ol-D_3) (v:v = 1:1) at a concentration of 50 mM. 10 μL of sample was added into the assembled Stark cell, which was immediately plunged into a custom-built cryostat that was filled with liquid nitrogen. The Stark cell was assembled using two calcium fluoride (CaF_2) optical windows (1 mm thick, 12.7 mm diameter, FOCtek Photonics) that were coated with nickel metal on one side (4.5 nm thick) and separated by Teflon spacers (26 μm thick). The Stark spectra were recorded on a Bruker Vertex 70 spectrometer at 1 cm^{-1} resolution with 64 scans in the presence of an applied electric field between 0.5 - 1.5 MV/cm. The external electric field was applied via a Trek 10/10 high-voltage

power amplifier. The results are shown in Supplementary Fig. 2a. Linear Stark tuning rates were obtained as previously described[1,13] from the contribution of the second-derivative component to the Stark spectrum (see Supplementary Table 4). The experimentally determined Stark tuning rate is reported as a product of the Stark tuning rate ($|\Delta\vec{\mu}|$) and the local field factor f, which reflects the difference between the applied electric field and the actual local electric field that is experienced by the vibrational probe.[1,14]

9. Vibrational solvatochromism

As described previously,[1] a demountable IR cell was assembled with two CaF_2 optical windows (19.05 mm diameter, 3 mm thick, Lambda Research Optics Inc.), which were separated by two Teflon spacers (25 μm and 50 μm thick). The sample was prepared by dissolving CXF in various solvents at low concentrations which typically ranged from 1 – 10 mM. 20 μL of sample was added into the IR cell, which was then tightly capped and wrapped with parafilm to minimize solvent evaporation and water absorption. The IR spectra were collected in a wavenumber window that spans 4000 cm^{-1} – 1000 cm^{-1} with 256 scans at 1 cm^{-1} resolution. The results are shown in Supplementary Fig. 2b and Supplementary Table 5.

10. Isotope-edited FTIR spectroscopy for LADH

To measure the carbonyl (C=O) frequency of CXF bound to LADH, the ^{13}C isotopically labeled compound, N-[^{13}C-formyl] cyclohexyl formamide (^{13}C-CXF) bound to LADH, was used as the background. As previously reported,[1] LADH was concentrated to ca. 1.6 mM with a total volume of ca. 60 μL, and then buffer exchanged into a D_2O buffer solution, containing either (1)

66 mM sodium phosphate, 100 mM potassium chloride at pD 8.20 or (2) 100 mM TES at pD 7.34. These two buffers gave the same IR spectra. 2 μL of a NADH solution (50 mM) was added into the protein sample, which was then split into two portions of ca. 25 μL, then 1 μL of CXF (40 mM) and ^{13}C-CXF (40 mM) were added into each portion. Similar to the solvatochromism experiments, 20 μL of the protein sample was injected into the assembled IR cell, and the IR spectra (4000 cm^{-1} – 1000 cm^{-1}) were collected with 512 scans at 1 cm^{-1} resolution. Nine spectra were collected from each sample for data analysis. The IR spectra of CXF, ^{13}C-CXF, and D_2O buffer were also collected for subtracting the IR signal of the unbound CXF from the protein spectra.

The procedure for data processing has been described in detail in previous work.[1,15] Briefly, the raw data in the form of transmission spectra were converted to absorption spectra. Then difference FTIR spectra were generated by subtracting the protein spectra with ^{13}C-CXF bound from that with CXF bound. A scaling factor was typically used to compensate for the difference of the background signal between the two spectra due to slight differences of the pathlength for each sample. In most cases, the scaling factor involved in this work was very close to unity (usually 0.95-1.05), indicating that the IR cell assemblies of isotope-labeled samples were highly consistent. The peak of the unbound inhibitor was subtracted from the difference FTIR spectrum, which was then minimally baseline corrected to give the final spectrum. All nine spectra were processed consistently as described above and analyzed using the built-in programs PeakPick and CurveFit in OPUS 5.0 to obtain the peak position and FWHM. The results shown in Supplementary Table 6 are the mean values over those nine spectra with one standard deviation as the corresponding error bar. These nine spectra were combined and averaged leading to the final spectral results shown in Figs. 2d & 3b, and Supplementary Fig. 3.

11. Enzyme kinetics

Ethanol dehydrogenation activity assay. The activity assay for screening metal ions for metal insertion is based on an established protocol.[16] Briefly, the activity buffer containing 85 mM sodium pyrophosphate, 6.5 mM semicarbazide·HCl, 18 mM glycine, and 550 mM ethanol at pH 9.0 was mixed with 1.75 mM NAD^+ on the same day of the experiment. The buffer was processed with Chelex 100 chelating resin as described above to remove any residual metal ions. To remove any residual metal ions in the quartz cuvette, we filled the cuvette with aqua regia and kept the interior soaked for 15 minutes before kinetic measurements. We then removed aqua regia and rinsed the cuvette with metal free Milli-Q water, which was also treated with the Chelex resin, at least ten times before drying the cuvette with air flow. For a typical activity measurement, 10 μL of 1 mg/mL (0.025 mM) LADH variant was added into 990 μL of the freshly prepared metal free activity buffer in the quartz cuvette. After rapid mixing, the sample was immediately put into a UV-Vis spectrometer to monitor the increase in the absorbance at 340 nm, which corresponds to the production of NADH [ε(340 nm) = 6.22 $mM^{-1}cm^{-1}$]. The reaction rate was calculated based on the slope of the kinetic trace. Three independent replicates were performed for each kinetic measurement. The results are shown in Supplementary Table 12.

Acetone hydrogenation kinetics. A fresh buffer containing 50 mM potassium phosphate and 1 mM NADH at pH 7.0 was prepared on the same day of the experiment. The buffer was processed with Chelex 100 chelating resin as described above to remove any residual metal ions. Because of the presence of 1 mM NADH in the kinetics buffer, we used a 0.1 cm pathlength quartz cuvette for kinetic measurements to ensure the absorbance at 340 nm is within the linear region that follows the Beer-Lambert law. The quartz cuvette for kinetic experiments was treated

with aqua regia as described above to remove any metal ions. The protein sample was buffer exchanged into a metal-free 50 mM potassium phosphate buffer at pH 7.0 with a protein concentration of about 0.25 mM. The protein concentration ($[E]_0$) for the wild type, $LADH^{S48T}$, and $LADH^{S48A}$ variants was determined based on the absorption at 280 nm using the extinction coefficient ε(280 nm) = 18 $mM^{-1}cm^{-1}$ from literature.[12] For metal exchanged LADH variants, i.e., $LADH^{Co}$, $LADH^{Cd}$, $LADH^{Co,S48T}$, and $LADH^{Co,S48A}$ variants, we first estimated their concentrations based on the amount of apo protein samples used for preparing them, and determined the final concentrations of those metal-exchanged variants based on ICP-OES elemental analysis (Methods section 4). For a typical kinetic measurement, 6 μL of the protein sample was rapidly mixed with 194 μL of a kinetic buffer containing varying amounts of acetone in a 1.5 mL Eppendorf tube before transferring the mixture into the cuvette, which was immediately put into the UV-Vis spectrometer for data collection. The cuvette was cleaned by rinsing with metal-free Milli-Q water and drying with air flow between different measurements. The change in the absorbance at 340 nm was recorded and the initial velocity (v_0) was obtained from the slope of the kinetic data. The kinetic data were fitted to the Michaelis-Menten kinetics model (Supplementary Fig. 5), from which we obtained the catalytic rate constant for acetone hydrogenation (k_{cat}) and the Michaelis constant (K_m) for acetone (Supplementary Table 8). Although the catalysis of acetone hydrogenation by LADH follows a bi bi ordered sequential mechanism[17] and therefore its steady-state kinetics can be described by a two-substrate Michaelis-Menten model (Eq. 1), this two-substrate model can be simplified to a single-substrate model (Eq. 2) in our kinetic studies, as also described in literature,[18] because the concentrations of the cofactor NADH (denoted as [NADH] in Eqs. 1 & 2) was kept constant during all the kinetic measurements at 1 mM, which is much higher

than its $K_{m,NADH}$ (2 μM) and $K_{i,NADH}$ (0.6 μM).[19] We further confirmed that 1 mM NADH is a saturating condition when acetone is the substrate (Supplementary Table 7). Three independent replicates for each protein variant were performed.

$$v_0/E_0 = \frac{k_{cat}[\text{NADH}][\text{acetone}]}{K_{i,\text{NADH}}K_{m,\text{acetone}} + K_{m,\text{NADH}}[\text{acetone}] + K_{m,\text{acetone}}[\text{NADH}] + [\text{acetone}][\text{NADH}]} \quad \text{(Eq. 1)}$$

$$v_0/E_0 = \frac{k_{cat}[\text{acetone}]}{K_{m,\text{acetone}} + [\text{acetone}]} \quad \text{(Eq. 2)}$$

Testing NADH saturation. A procedure similar to that of acetone hydrogenation kinetics was performed, except for keeping the acetone concentration constant but varying the NADH concentration. The initial rates of acetone hydrogenation were recorded and compared. The results are shown in Supplementary Table 7.

Benzaldehyde hydrogenation kinetics. A procedure similar to that of acetone hydrogenation kinetics was performed, except for using benzaldehyde as the substrate. The kinetic data were fitted to Michaelis-Menten kinetics model (Supplementary Fig. 6a-c), from which we obtained the catalytic rate constant for benzaldehyde hydrogenation (k_{cat}) and the Michaelis constant (K_m) for benzaldehyde (Supplementary Table 9).

CXF competitive inhibition kinetics. We chose benzaldehyde as the substrate for studying the competitive inhibition of LADH by CXF, because benzaldehyde's kinetic parameters are suitable for this measurement. A procedure similar to that of benzaldehyde hydrogenation kinetics was performed, except we kept the concentration of benzaldehyde constant and varied the concentration of CXF added into the reaction mixture. By recording the initial rates of benzaldehyde hydrogenation as a function of CXF concentration, we obtained the K_i of CXF by

non-linear fitting according to the competitive inhibition kinetic equation (Eq.3), where v_0 is the initial rate, and $[E]_0$, [S], and [I] are the concentration of LADH, benzaldehyde, and CXF, respectively. The values of [S] were chosen as 400 μM, 1 mM, and 10 mM for WT, S48T, and S48A, respectively. The data fitting and the results are presented in Supplementary Fig. 6d-f and Supplementary Table 9.

$$\frac{v_0}{[E]_0} = \frac{k_{cat}\,\frac{[S]}{K_M}}{1 + \frac{[S]}{K_M} + \frac{[I]}{K_i}} \qquad \text{(Eq. 3)}$$

Isopropanol dehydrogenation kinetics. A fresh buffer containing 50 mM potassium phosphate, 8 mM semicarbazide·HCl, and 2 mM NAD^+ at pH 7.0 was prepared on the same day of the experiment. Semicarbazide·HCl has been extensively used in previous studies of LADH kinetics[12,18] to trap the product acetone and thus prevent the reversible reaction (see Supplementary Text 4). Both kinetic buffer and the quartz cuvette were pretreated as described above to avoid any metal ion contamination. The cuvette for isopropanol dehydrogenation kinetics has a pathlength of 1.0 cm, and the protein sample was buffer exchanged into a metal-free 50 mM potassium phosphate buffer at pH 7.0 with a protein concentration of about 0.06 mM. Protein concentration was determined the same way as described above. For a typical kinetic measurement, 5 μL of the protein sample was rapidly mixed with 495 μL of kinetic buffer containing varying amounts of acetone in the cuvette by quickly inverting the cuvette a few times, which was then immediately put into a UV-Vis spectrometer. The cuvette was cleaned by rinsing with metal-free Milli-Q water and drying with air flow between different measurements. The change in the absorbance at 340 nm was recorded and the initial velocity was obtained from

the slope of the kinetic data. The kinetic data were fitted to Michaelis-Menten kinetics model (Supplementary Fig. 8), from which we obtained the catalytic rate constant for isopropanol dehydrogenation (k_{cat}) and the Michaelis constant (K_m) for isopropanol (Supplementary Table 8). Three independent replicates for each protein variant were performed.

Supplementary Texts

Text 1. Why we studied acetone reduction kinetics in this work

Because we are focused on studying the effect of the active-site electric field on the chemical step of LADH catalysis, which is hydride transfer, we need to choose an LADH-catalyzed reaction that is rate limited by hydride transfer as the model reaction. Although LADH can catalyze the transformation of a wide range of aldehyde substrates, it is known that for aldehyde substrates the steady-state kinetics of LADH is rate limited by the product dissociation step rather than the hydride transfer[12,20-22]. Even transient kinetic studies of acetaldehyde reduction using the stopped-flow technique were unable to determine the hydride transfer rate[12,20-22]. The apparent maximum rate constant ($k_{\max}$) obtained from the transient reduction kinetics of aldehydes showed practically no kinetic isotope effect[12], which indicates that the measured $k_{\max}$ is not rate limited by hydride transfer.

Given the complexity of aldehyde reduction kinetics by LADH, we chose to study the acetone reduction kinetics. It has been shown that the steady-state kinetics of LADH-catalyzed acetone reduction is rate limited by hydride transfer[23,24]. This allows us to directly and reliably measure the hydride transfer rate based on Michaelis-Menten kinetic studies. We focused on acetone reduction instead of its reverse reaction, isopropanol oxidation, because the electric field measured by our carbonyl probe is most directly related to the reduction pathway as discussed in Supplementary Text 4.

Another advantage of using acetone for measuring kinetics is that acetone's transition state analogue, dimethylsulfoxide (DMSO), has been co-crystallized with LADH and NADH[25], which

shows a similar alignment of the S=O as compared to that of C=O in CXF (Supplementary Fig. 4). This supports our hypothesis that the electric fields probed by CXF can recapitulate the fields experienced by acetone when it enters the transition state, reinforcing the link between electric field and free energy barrier.

Text 2. Comparison of binding constants between the substrates and the inhibitor

The most striking difference is that acetone binds in the mM range while benzaldehyde and CXF bind in the μM range (Supplementary Table 10), and acetaldehyde's K_M[26] is in the intermediate sub-mM range. There are two possible origins for these differences in binding constant. (a) Compared with the three aldehydes, acetone bears a methyl group directly connected to the C=O, which contributes to a large steric hindrance. This agrees well with the literature[23,24] that ketones bind worse than aldehydes; (b) Compared with acetaldehyde, benzaldehyde and CXF both carry functional groups that introduce additional interactions with the protein. Our results indicate that for aldehyde, -(H)C=O, functional groups on the other side of the hydrogen atom promote the binding by forming more interactions, rather than inhibiting the binding due to more steric hinderance. The high binding affinity of CXF further validates the conditions of our IR experiments where we used CXF at mM concentrations.

Going from WT to S48T to S48A, we observed a trend of increase in binding constant across acetone, acetaldehyde, benzaldehyde, and CXF. One exception is that the binding of acetone by S48T is weaker than that by S48A.

Text 3. Slope and intercept of the line of electrostatic catalysis

By extrapolating the linear fit of the free energy barrier and the active-site electric field (Fig. 4f) to zero field, one obtains an estimate for the activation energy for a hypothetical enzyme that projects no electric field onto the reaction C=O bond but retains the well-positioned NADH for hydride transfer. The obtained intercept gave a free energy barrier for the zero-field enzyme of 38.0 kcal/mol, indicating an intrinsically difficult reaction when not promoted by electric fields; however, this reaction has a large catalyzability by electric fields, meaning that electrostatic catalysis is productive in lowering the barrier. The catalyzability is manifested by the value of the slope of the linear fitting, giving the reaction difference dipole, $(\vec{\mu}_{\mathrm{TS}} - \vec{\mu}_{\mathrm{RS}})$ = 2.38 D (see Fig. 1c). As a result, the large projection of the electric field (-165 MV/cm) in LADH substantially lowers the barrier by 18.6 kcal/mol. For comparison, KSI has a lower reaction difference dipole of 1.05 D; its similarly large electric field (-144 MV/cm) only produces a barrier lowering of 7.3 kcal/mol. The large intercept and the large slope of the linear of electrostatic catalysis for LADH indicates the importance and the dramatic effect of electric fields, leading to a system suitable for electric field optimization and enzyme design.

Text 4. Bi-directional hydride transfer catalyzed by LADH.

It has long been observed that many enzymes can catalyze reactions reversibly,[27] i.e., they achieve rate accelerations in both reaction directions. This catalytic reversibility has gained substantial interest because of its promising applications in energy conversion and storage.[28,29] As

discussed in the main text, our work has been largely focused on the direction of hydride transfer that converts an aldehyde/ketone to an alcohol because the IR probe we used for measuring electric fields is an aldehyde-analog inhibitor. The activation energy of this reaction has been carefully calculated in literature[30]. Unlike acetone hydrogenation, where the hydride transfer is rate limiting, alcohol dehydrogenation involves a proton transfer step either (a) prior to the hydride transfer[31,32] or (b) those steps could be essentially concerted because of the low-barrier H bond between the S48 residue O and the alcohol OH as indicated by inverse solvent isotope effects[12]. For mechanism (a), previous studies[31,32] suggest that the free energy barrier of this proton transfer is comparable to that of the following hydride transfer, and as a result, the measured k_{cat} of isopropanol dehydrogenation may reflect a convolution of both proton and hydride transfers. For mechanism (b), mutation to S48 may disrupt the low-barrier H-bond between the S48 residue O and the alcohol OH and lead to different mechanisms for different mutants. Therefore, both scenarios complicate a direct correlation between the kinetics and the electric fields. Moreover, the electric field we measured using the carbonyl probe could be different from that experienced by the alcohol C-O bond, which we are unable to probe. For these reasons, it is not appropriate to directly correlate the free energy barrier of the alcohol dehydrogenation with the electric fields we measured for CXF's C=O. Nevertheless, for completeness we report the Michaelis-Menten kinetics of the dehydrogenation of isopropanol as shown in Supplementary Table 8 and Supplementary Fig. 8.

Supplementary Figures

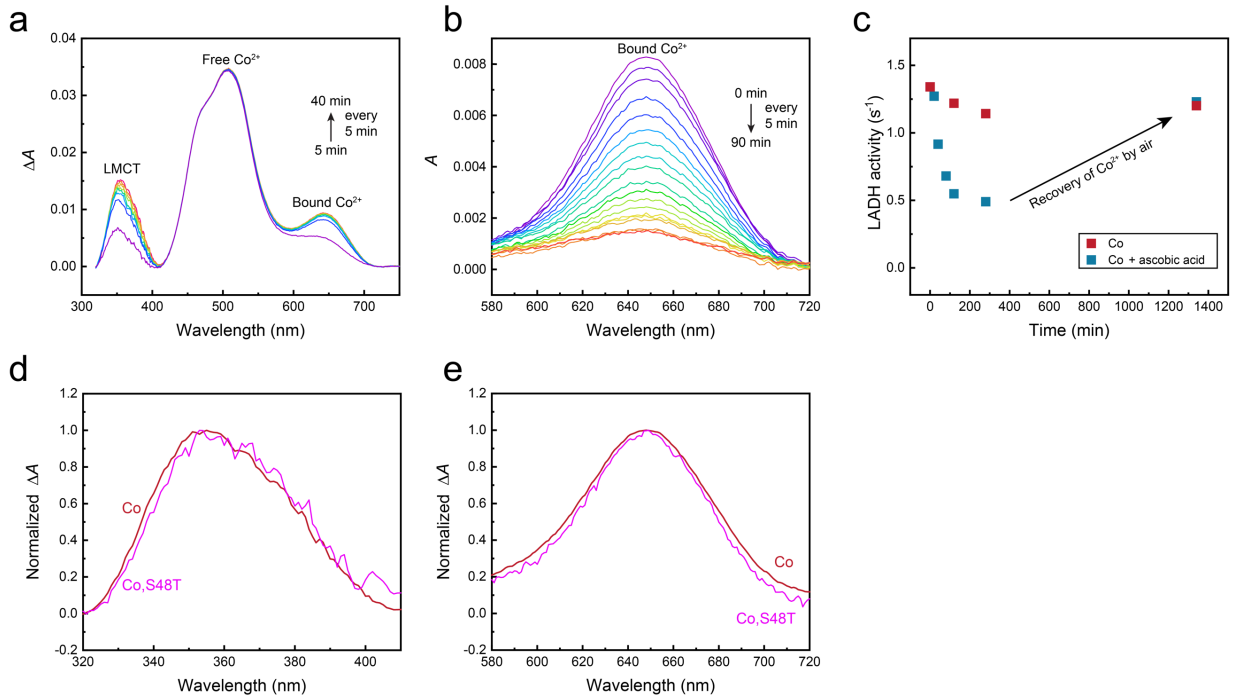

Supplementary Fig. 1. Co^{2+} insertion and reduction in LADH. **a**, Time evolution of the UV-Vis spectrum of 28 μM apo-LADH upon adding 5 mM cobalt acetate. Shown here are the difference spectra taken by subtracting the cobalt-free absorbance from the cobalt-containing one for better display of the ligand-metal charge transfer (LMCT) peaks. The formation of $LADH^{Co}$ was characterized by the UV-Vis absorptions rising at 648 and 354 nm, corresponding to the d-d transition of the Co^{2+} and the S(Cys) → Co^{2+} charge transfer, respectively, at the active site.[3,10] **b**, Time evolution of the Vis spectrum of 28 μM $LADH^{Co}$ treated with 20 mM ascorbic acid. The decrease in the absorption at 648 nm indicates the reduction of the bound Co^{2+} in the active site. **c**, Time evolution of $LADH^{Co}$'s activity for ethanol dehydrogenation with and without being treated with 20 mM ascorbic acid. After 1,340 min, the activity was recovered because of the oxidation of Co^{1+} to Co^{2+} by air after ascorbic acid is depleted by $LADH^{Co}$-mediated oxidation by air. **d,e**, UV-Vis spectra of $LADH^{Co}$ and $LADH^{Co,S48T}$ showing the same absorption at 354 nm (d) and 648 nm (e). Shown here are the difference spectra taken by subtracting the cobalt-free absorbance from the cobalt-containing one for better display of the peaks.

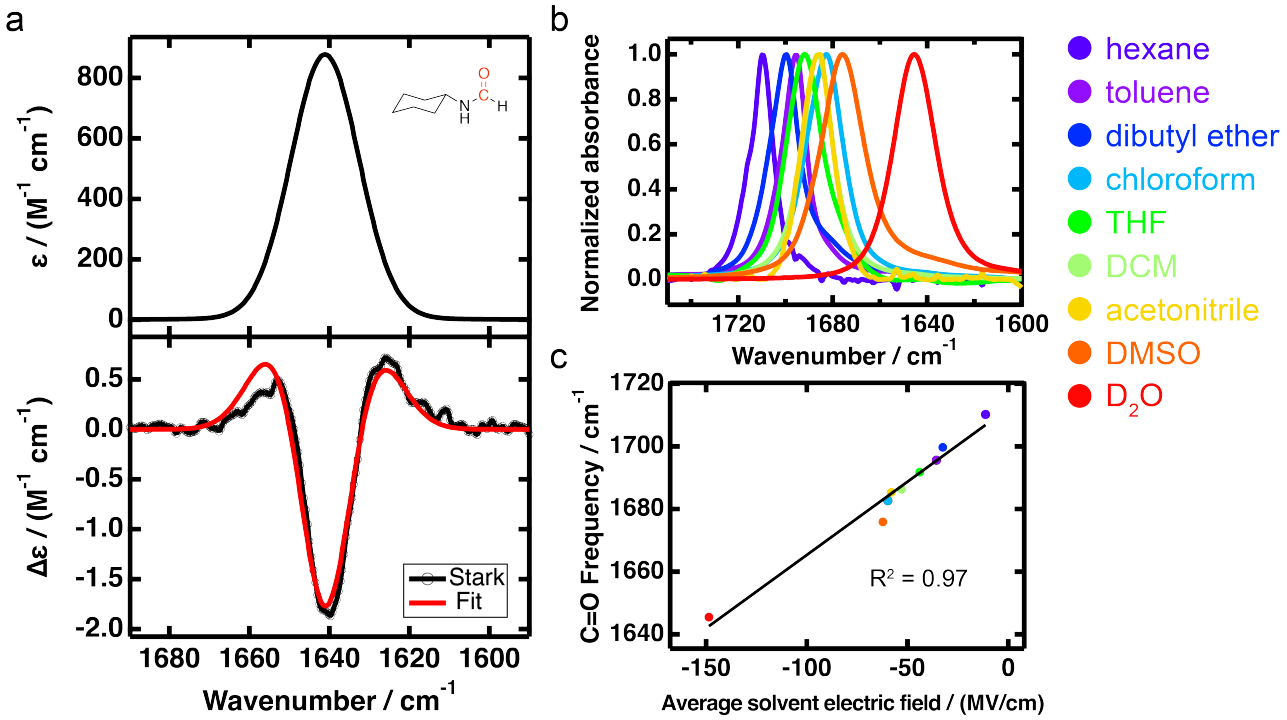

Supplementary Fig. 2. Calibration of the carbonyl (C=O) of CXF as a vibrational probe for measuring electric fields. a, Vibrational Stark spectroscopy of 50mM CXF in a mixture of D_2O and glycer(ol-d_3) (v:v = 1:1) at 77 K. The top panel is the absorption spectrum of the C=O of CXF; the bottom panel shows the corresponding vibrational Stark spectrum scaled to an applied field of 1.0 MV/cm with best fits (red line). **b,** Normalized infrared (IR) spectra of the C=O of CXF dissolved in various solvents with different polarities. **c,** A linear correlation between the measured IR frequencies of C=O in solvents (Supplementary Table 5) and the average solvent electric fields exerted on the C=O bond as calculated by SPADE QM combined with fixed-charge MD in our previous study[1] (reproduced in Supplementary Table 5). The standard errors of the computed solvent electric fields are quite small (Supplementary Table 5). The linear correlation, $\bar{\nu}_{C=O} = 0.47F_{C=O} + 1712.2$ $(R^2 = 0.97)$, enables the mapping of the observed C=O's IR frequency to the electric field projected on it based on the vibrational Stark effect. Note that the electric field calculations in ref. 1, which are also reproduced here, use *N*-[formyl-^{2}H]-CXF (CXF-D), a deuterated aldehyde, rather than CXF as the solute. This is a reasonable approximation because we found that the solvent electric fields experienced by the C=O of CXF and that of CXF-D are quite similar as expected based on our simulation results using fixed-charge MD (Supplementary Table 5). CXF-D's IR spectra are slightly different from that of CXF due to a small secondary effect on the carbonyl stretch frequency.

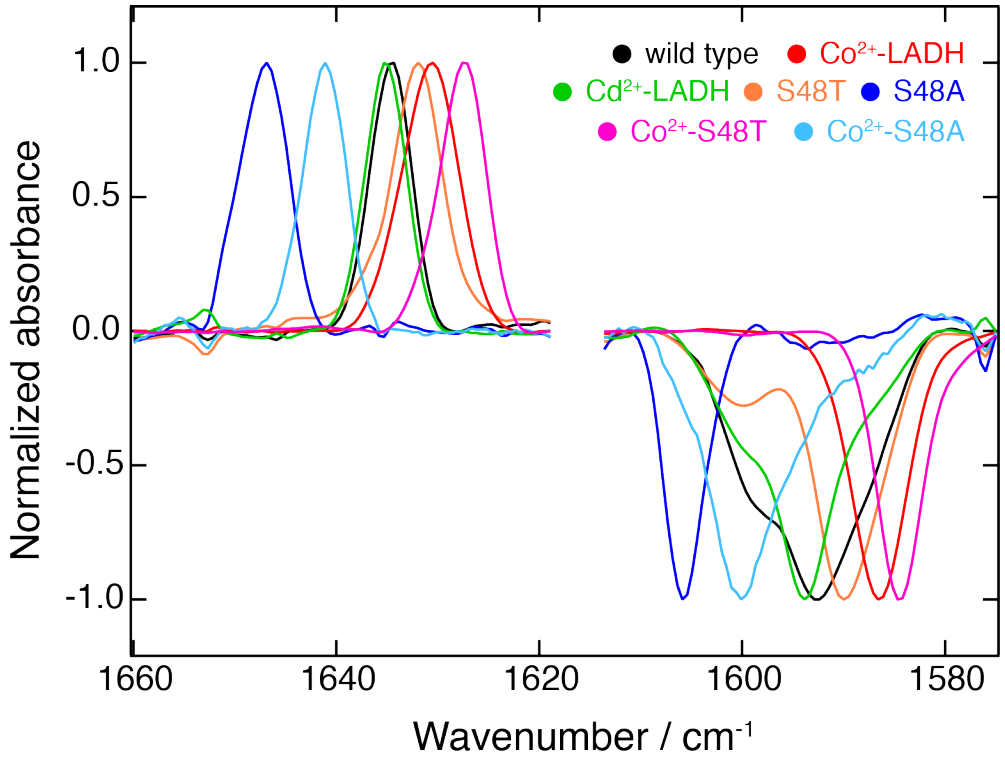

Supplementary Fig. 3. Normalized infrared spectra of the carbonyl of CXF bound to LADH, forming a ternary complex of LADH:NADH:CXF. These normalized difference spectra were obtained by subtracting the spectra of ^{13}C-CXF in the ternary complex from that of CXF under the same conditions; this isotope-edited method removes the infrared background arising from the protein amide backbone. The positive and negative peaks correspond to the carbonyls of CXF and ^{13}CXF, respectively, which are separated by approximately 40 cm^{-1} due to the isotope effect (Supplementary Table 6). The ^{13}C=O of bound ^{13}C-CXF in some cases shows a shoulder peak around 1600 cm^{-1} which may be due to a Fermi resonance.

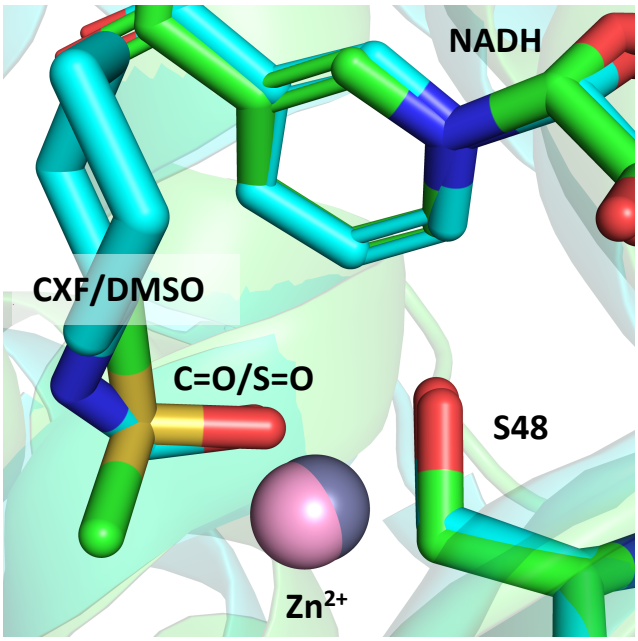

Supplementary Fig. 4. Crystal structure overlay between the DMSO and CXF bound LADH-NADH. The structures with DMSO (PDB: 2OHX[25]) and CXF (PDB: 7RM6[1]) are shown in green and cyan, respectively. The Zn^{2+} ions in the DMSO and the CXF structures are shown in gray and pink, respectively. The S=O in DMSO and the C=O in CXF are labeled. The two structures are aligned based on these active site elements.

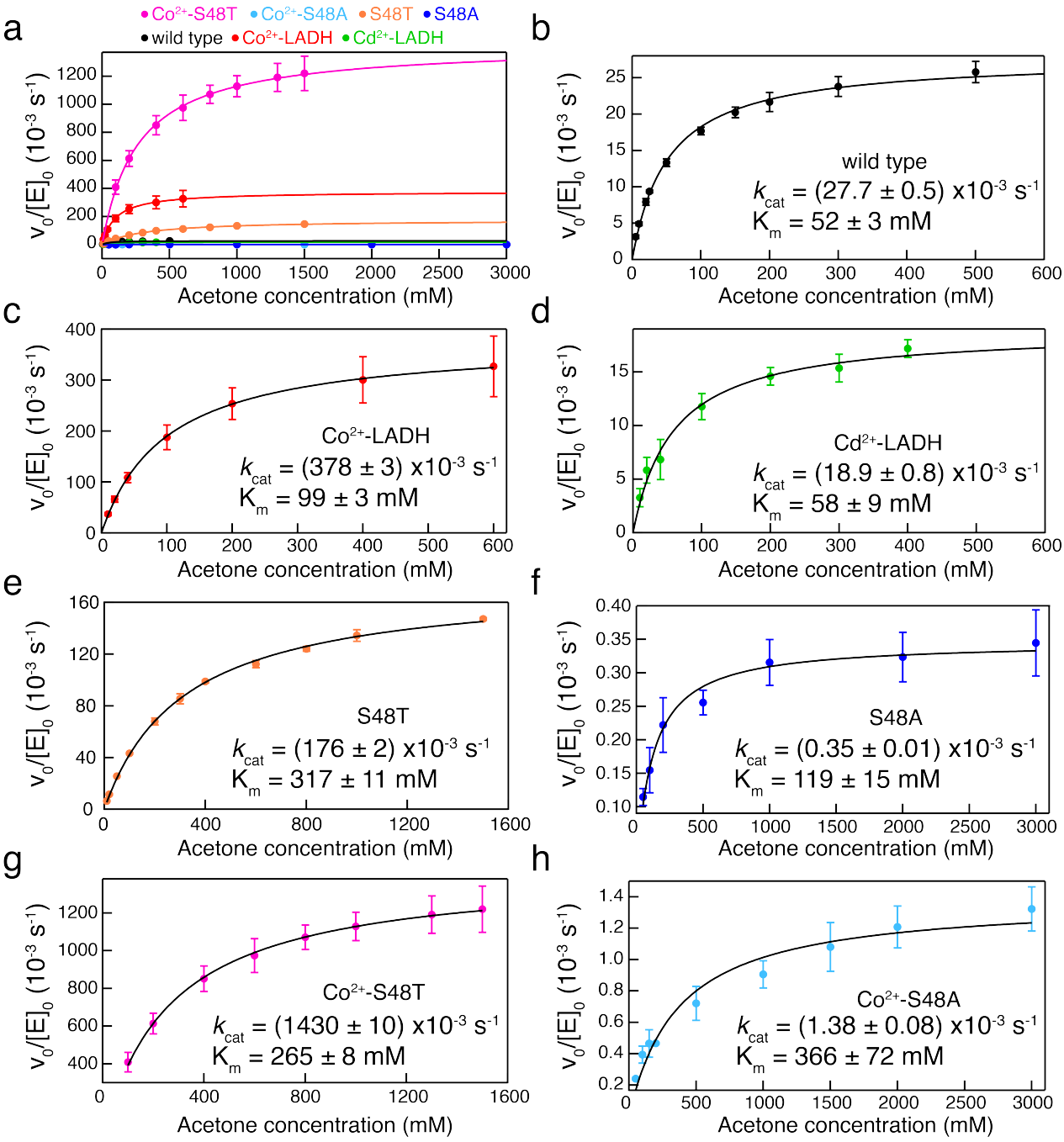

Supplementary Fig. 5. Michaelis-Menten kinetics of acetone hydrogenation catalyzed by LADH. The kinetic data (y axis) are presented as mean values +/- SD based on n=3 independent replicates. Panel (**a**) shows the kinetic curves of all seven LADH variants in this work. Panels (**b**) – (**h**) show the kinetic curves of each individual LADH variant. The reported errors associated with k_{cat} and K_m (Supplementary Table 8) represent one standard error of the curve fitting.

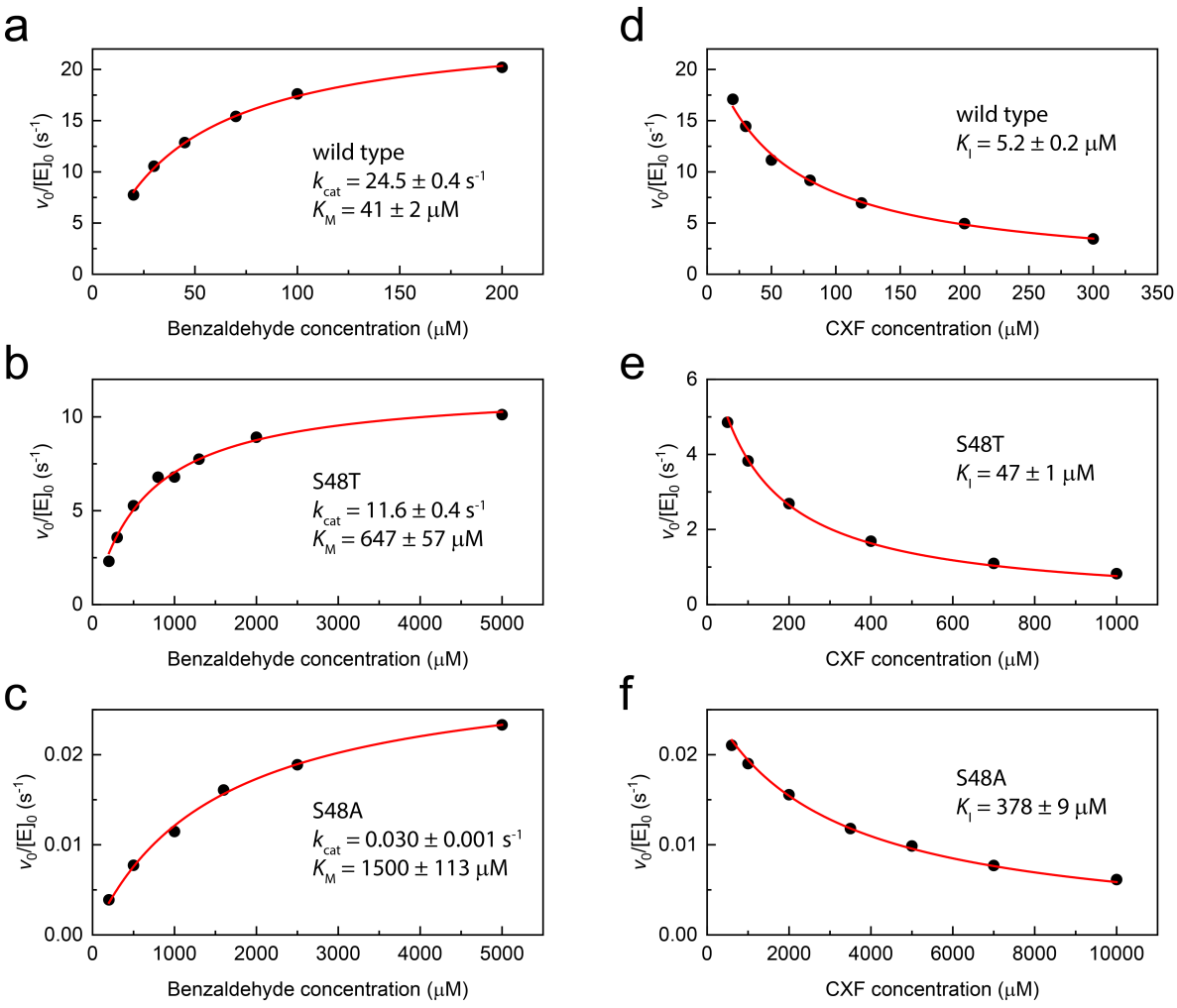

Supplementary Fig. 6. Michaelis-Menten kinetics of benzaldehyde hydrogenation by LADH and competitive inhibition by CXF. Panels (**a-c**) show the Michaelis-Menten kinetics of benzaldehyde hydrogenation by WT, S48T, and S48A mutants of LADH, respectively. Panels (**d-f**) show CXF's competitive inhibition of benzaldehyde hydrogenation by WT, S48T, and S48A mutants of LADH. K_i was obtained by non-linear fitting according to the competitive inhibition kinetic equation, $\frac{v_0}{[E]_0} = \frac{k_{cat}\frac{[S]}{K_M}}{1+\frac{[S]}{K_M}+\frac{[I]}{K_i}}$, where v_0 is the initial rate, and $[E]_0$, [S], and [I] are the concentration of LADH, benzaldehyde, and CXF, respectively. The values of [S] were chosen as 400 μM, 1 mM, and 10 mM for WT, S48T, and S48A, respectively. The reported errors associated with k_{cat}, K_M, and K_i (Supplementary Table 9) represent one standard error of the curve fitting.

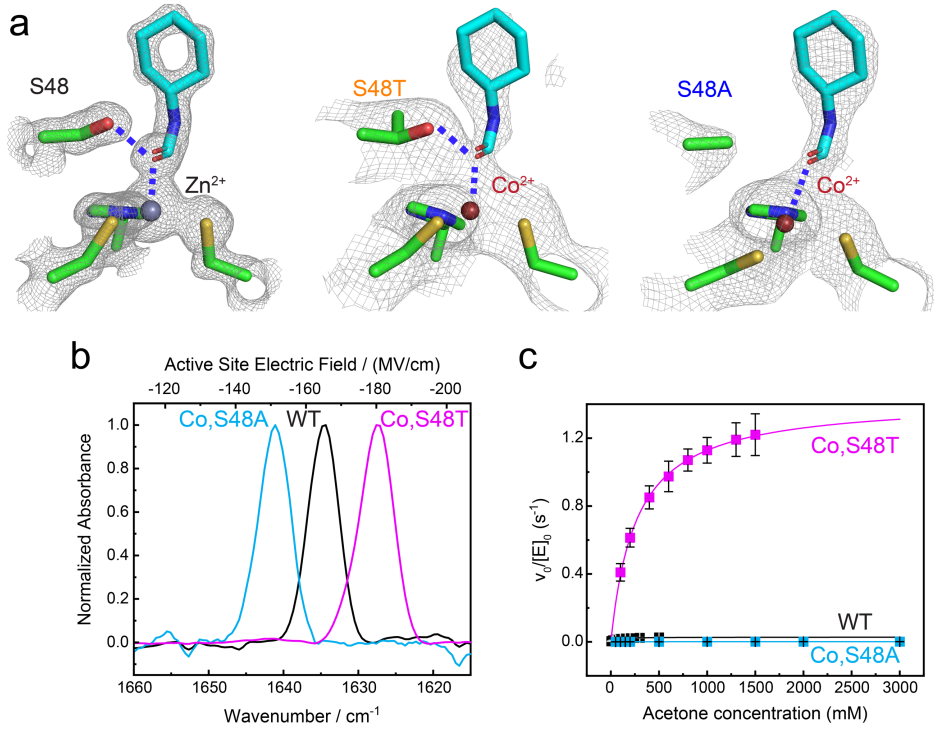

Supplementary Fig. 7. Double mutants of LADH. a, X-ray structures of wildtype LADH at 1.43 Å resolution (7RM6), LADH^{Co,S48T} at 2.55 Å resolution (8EIY), and LADH^{Co,S48A} at 2.46 Å resolution (8EIX). **b**, Infrared spectra of the C=O in CXF bound to the active site of wildtype LADH, LADH^{Co,S48T}, and LADH^{Co,S48A}. See Fig. 2d caption for details. **c**, Michaelis-Menten kinetics of acetone hydrogenation by wildtype LADH, LADH^{Co,S48T}, and LADH^{Co,S48A}. See Fig. 2e caption for details.

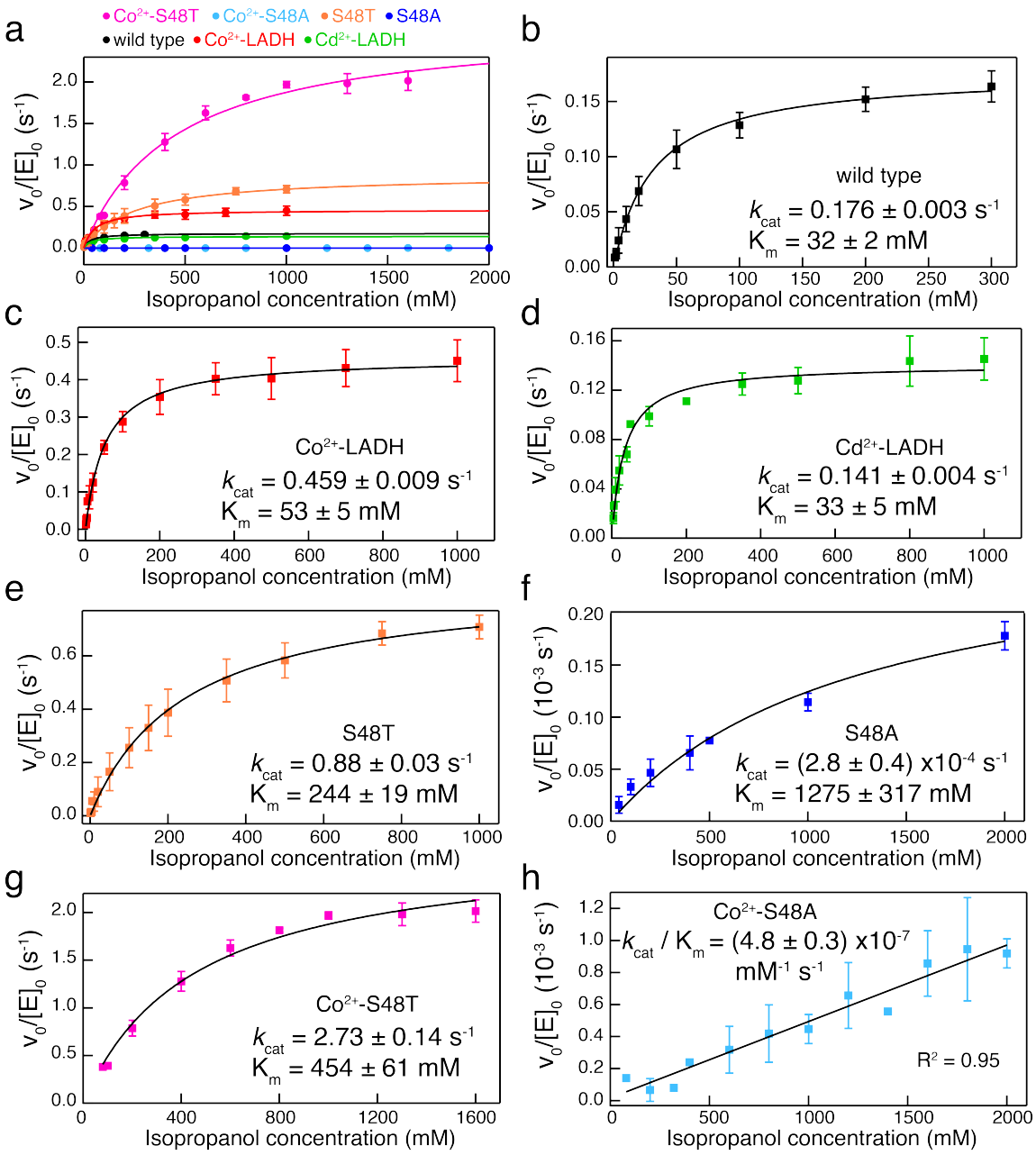

Supplementary Fig. 8. Michaelis-Menten kinetics of isopropanol dehydrogenation catalyzed by LADH. The kinetic data (y axis) are presented as mean values +/- SD based on n=3 independent replicates. Panel (**a**) shows the kinetic curves of all seven LADH variants in this work. Panels (**b**) – (**g**) show the kinetic curves of each individual LADH variant except for LADH^{Co,S48A}. The reported errors associated with k_{cat} and K_m (Supplementary Table 8) represent one standard error of the curve fitting. Panel (h) shows the kinetic curve of LADH^{Co,S48A}, for which the k_{cat} and K_m cannot be determined because the reaction rate does not plateau with 2 M isopropanol and using a higher isopropanol concentration was found to denature LADH. A linear fitting to these data gave k_{cat} / K_m of this mutant, and the reported error associated with k_{cat} / K_m denotes one standard error of the linear fitting.

Supplementary Tables

Supplementary Table 1. Native mass spectrometry of LADH variants

LADH Variant	Calculated MS (dimer) Da	Measured MS[a] Da
Apo LADH	80109.8	80106.8
Wildtype $LADH^{Zn}$	80240.5	80233.3
$LADH^{Co}$	80227.6	80222.9
$LADH^{Cd}$	80334.6	80329.7

[a] The measured mass has a systematic error within 10 Da, depending on instrument status.

Supplementary Table 2. Metal ratios in LADH variants measured by ICP-AES

LADH Variant	M/Zn Ratio[a,b]
$LADH^{Co}$	0.74 ± 0.12
$LADH^{Co,S48A}$	0.87 ± 0.06
$LADH^{Co,S48T}$	0.56 ± 0.03
$LADH^{Cd}$	1.01 ± 0.13

[a] The molar ratio of the number of the inserted metal in the active site to the fixed number of the structural Zn.

[b] Data are presented as mean values +/- SD based on the measurements of n=3 independent samples.

Supplementary Table 3. X-ray diffraction data collection and refinement statistics

Protein	**LADH^{S48T}**	**LADH^{Co}**	**LADH^{Cd}**	**LADH^{S48A}**	**LADH^{Co,S48T}**	**LADH^{Co,S48A}**
PDB entry	7UQ9	8EIW	7UTW	7U9N	8EIY	8EIX
Data collection statistics						
Beamline	BL 12-2	BL 12-2	BL 12-1	BL 12-2	BL12-2	BL 12-2
Wavelength (Å)	0.979	0.979	0.979	0.979	0.979	0.979
Resolution range (Å)	38.26 – 1.40 (1.42 – 1.40)	39.12 – 1.65 (1.69 – 1.65)	38.02 – 1.33 (1.35 – 1.33)	38.13 – 2.20 (2.25 – 2.20)	39.09 – 2.55 (2.67 – 2.55)	37.36 – 2.46 (2.52 – 2.46)
Space group	P 1	P 1 21 1	P 1	P 1	P 1 21 1	P 1
Unit cell dimensions a, b, c, (Å) α, β, γ (°)	44.36, 51.27, 92.82 92.37, 103.03, 109.50	54.96, 71.64, 92.68 90.00, 102.98, 90.00	44.21, 50.81, 92.90 92.39, 102.93, 109.33	54.91, 68.66, 94.40 89.65, 76.00, 88.99	55.10, 71.54, 92.44 90.00, 102.95, 90.00	56.27, 57.56, 68.25 72.32, 74.88, 71.60
Matthews coefficient	2.27	2.10	2.24	2.16	2.09	2.32
Solvent content (%)	45.8	41.4	45.2	42.97	41.3	46.9
Total observations	984107 (44642)	1138596 (82455)	1155326 (50726)	474125 (31749)	155570 (11971)	188569 (13531)
Unique observations	130465 (6446)	84133 (6195)	150446 (7025)	61757 (4287)	22067 (1651)	27150 (1993)
Multiplicity	7.5 (6.9)	13.5 (13.3)	7.7 (7.2)	7.7 (7.4)	7.1 (7.3)	6.9 (6.8)
Completeness (%)	88.8 (87.3)	99.7 (99.4)	88.5 (83.4)	90.6 (85.1)	95.7 (96.8)	98.1 (97.9)
Mean I/σ(I)	9.2 (1.5)	12.1 (1.4)	16.1 (2.2)	9.7 (1.4)	9.4 (1.8)	9.4 (1.5)
Wilson B-factor (Å^2)	13.0	21.1	11.1	36.8	48.9	57.1
Anisotropy	0.543	0.480	0.429	0.346	0.686	0.058
R_{merge}	0.110 (1.299)	0.123 (2.105)	0.071 (1.035)	0.131 (1.628)	0.154 (1.654)	0.139 (1.964)
R_{meas}	0.118 (1.404)	0.127 (2.188)	0.076 (1.113)	0.140 (1.749)	0.166 (1.780)	0.150 (2.130)
$CC_{1/2}$	0.987 (0.704)	0.999 (0.658)	0.999 (0.828)	0.998 (0.625)	0.998 (0.734)	0.997 (0.635)
Refinement statistics						
Reflections used	130355	84080	150245	61679	22027	27143
Reflections used for R_{free}	6517	4215	7516	3127	1106	1367
R_{work}	0.1561	0.1784	0.1376	0.2132	0.2077	0.2060
R_{free}	0.1834	0.2050	0.1650	0.2587	0.2634	0.2437
Number of non-H atoms	6691 5572	6275 5573	6766 5570	11622 11136	5718 5572	5705 5568

Protein Ligand Solvent	110 1009	110 592	110 1086	220 266	101 45	110 27
Protein residues	756	756	756	1512	755	756
RMSD bond lengths (Å)	0.007	0.012	0.016	0.011	0.006	0.006
RMSD bond angles (°)	1.02	1.13	1.39	1.34	0.90	0.97
Ramachandran favored (%)	97.04	97.04	97.04	96.03	93.28	93.01
Ramachandran allowed (%)	2.96	2.96	2.96	3.70	6.45	6.45
Ramachandran outliers (%)	0.00	0.00	0.00	0.27	0.27	0.54
Rotamer outliers (%)	0.00	0.65	0.65	2.77	0.81	0.33
Clashscore	2.53	2.70	2.79	12.01	10.14	8.73
Average B factor ($Å^2$) Protein Ligand Solvent	21.01 18.82 15.26 33.75	28.54 27.75 23.56 36.87	19.04 16.38 13.51 33.27	51.37 51.60 43.87 47.88	59.20 59.32 55.44 53.20	66.18 66.33 60.16 59.43

[a] Statistics for the highest-resolution shell are shown in parentheses.

Supplementary Table 4. Vibrational Stark effect data (Supplementary Fig. 2a)

Compound	Vibrational mode	Conc. M	Solvent	Peak position cm^{-1}	FWHM cm^{-1}	A[a]	B cm^{-1}	C cm^{-2}	$\|\Delta\vec{\mu}\|f$ cm^{-1} / (MV/cm)
N-cyclohexyl formamide	C=O	0.05	D_2O:glycer(ol-D_3) (v/v 1/1)	1641.09	20.1	-2.48 × 10^{-4}	6.57 × 10^{-4}	1.27 × 10^{-1}	1.13

[a] A, B, and C are the fitting coefficients for the Stark spectra, corresponding to the 0th (A), 1st (B), and 2nd (C) derivative contributions, respectively.[14] The Stark tuning rate ($|\Delta\vec{\mu}|f$) can be extracted from the coefficient of the 2nd derivative contribution (C) assuming the difference dipole of the vibrational mode is parallel with its transition dipole moment.

Supplementary Table 5. Calibration of vibrational probe, the C=O in CXF (Supplementary Fig. 2c)

Solvent	CXF		CXF-D	CXF-D	CXF
	IR		SPADE-FC[a]	FC[b]	FC[b]
	Peak position cm^{-1}	FWHM cm^{-1}	Average solvent electric field[c] MV/cm		
Hexane	**1710.2**	11.4	**-11.3 ± 0.4**	-0.22 ± 0.01	-0.21 ± 0.01
Toluene	**1695.6**	12.4	**-35.7 ± 0.8**	-25.69 ± 0.11	-25.17 ± 0.11
Dibutyl ether	**1699.7**	15.2	**-32.6 ± 0.9**	-18.30 ± 0.11	-19.28 ± 0.11
Chloroform	**1682.7**	18.8	**-59.8 ± 1.7**	-44.16 ± 0.19	-45.39 ± 0.19
THF	**1691.8**	18.6	**-44.0 ± 1.0**	-31.94 ± 0.13	-32.57 ± 0.13
DCM	**1686.3**	15.6	**-53.0 ± 1.3**	-45.72 ± 0.17	-44.60 ± 0.17
Acetonitrile	**1685.3**	15.6	**-58.1 ± 1.4**	–	–
DMSO	**1675.9**	21.9	**-62.2 ± 1.4**	-54.40 ± 0.18	-54.38 ± 0.17
D_2O	**1645.5**	21.1	**-148.6 ± 3.4**	-108.98 ± 0.31	-108.49 ± 0.31

[a] The solvent electric fields were computed using the SPADE QM partitioning method with solute-solvent configurations sampled from fixed-charge MD.[1] The results are reproduced from ref. 1. These values (in green) were used for the linear calibration of the vibrational probe as shown in Supplementary Fig. 2c.

[b] The solvent electric fields were computed via fixed-charge MD using the intrinsic parameters of GAFF.[1] The results are reproduced from ref. 1.

[c] Data are presented as mean values +/- SE based on n=5000 frames from an MD trajectory.

Supplementary Table 6. Isotope-edited infrared spectra of *N*-cyclohexylformamide bound to LADH and the measured electric fields in the active site of LADH variants (Supplementary Fig. 3)

LADH variants	^{12}C=O		^{13}C=O	
	Peak position cm^{-1}	FWHM cm^{-1}	Peak position cm^{-1}	FWHM cm^{-1}
Wildtype LADH^{Zn}	1634.6 ± 0.2	4.8 ± 0.1	1592.7 ± 0.1	13.9 ± 0.4
LADH^{Co}	1630.58 ± 0.03	6.6 ± 0.1	1586.7 ± 0.2	6.4 ± 0.1
LADH^{Cd}	1635.17 ± 0.04	4.8 ± 0.1	1594.1 ± 0.3	8.5 ± 0.5
LADH^{S48T}	1631.9 ± 0.1	5.7 ± 0.2	1590.0 ± 0.1	6.97 ± 0.06
LADH^{S48A}	1646.91 ± 0.03	5.8 ± 0.2	1605.79 ± 0.03	4.6 ± 0.1
LADH^{Co,S48T}	1627.38 ± 0.06	5.4 ± 0.3	1584.6 ± 0.2	5.4 ± 0.2
LADH^{Co,S48A}	1641.6 ± 0.2	4.9 ± 0.4	1600.2 ± 0.4	8.6 ± 0.5

Data are presented as mean values +/- SD of the peak picking results based on at least nine technical replicates, from which the obtained spectra were independently processed (Supplementary methods section 11).

Supplementary Table 7. Testing the saturation condition of NADH in acetone hydrogenation by WT LADH

Acetone concentration mM	NADH concentration μM	Rate of acetone hydrogenation s^{-1}
500	1000	0.030
500	200	0.031
500	50	0.029

Supplementary Table 8. Michaelis-Menten kinetics of acetone hydrogenation and isopropanol dehydrogenation by LADH

	Acetone hydrogenation[a]			Isopropanol dehydrogenation[a]		
LADH variants	k_{cat} 10^{-3} s^{-1}	K_m mM	k_{cat}/K_m M^{-1} s^{-1}	k_{cat} 10^{-3} s^{-1}	K_m mM	k_{cat}/K_m M^{-1} s^{-1}
Wildtype $LADH^{Zn}$	27.7 ± 0.5	52 ± 3	0.53 ± 0.04	176 ± 3	32 ± 2	5.5 ± 0.4
$LADH^{Co}$	378 ± 3	99 ± 3	3.8 ± 0.1	459 ± 9	53 ± 5	8.7 ± 1.0
$LADH^{Cd}$	18.9 ± 0.8	58 ± 9	0.32 ± 0.06	141 ± 4	33 ± 5	4.3 ± 0.8
$LADH^{S48T}$	176 ± 2	317 ± 11	0.56 ± 0.03	880 ± 30	244 ± 19	3.6 ± 0.4
$LADH^{S48A}$	0.35 ± 0.01	119 ± 15	0.0029 ± 0.0004	0.28 ± 0.04	1275 ± 317	0.00022 ± 0.00009
$LADH^{Co,S48T}$	1430 ± 10	265 ± 8	5.4 ± 0.2	2730 ± 140	454 ± 61	6.0 ± 1.1
$LADH^{Co,S48A}$	1.38 ± 0.08	366 ± 72	0.0038 ± 0.0010	N/A[b]	$\gg 2000$[b]	0.00048 ± 0.00003

[a] The reported errors associated with k_{cat} and K_m represent one standard error of the Michaelis-Menten curve fitting based on three independent replicates. The errors associated with k_{cat}/K_m are based on the error propagations from k_{cat} and K_m except for $LADH^{Co,S48A}$, whose error was determined by one standard error of the linear fitting based on three independent replicates. [b] The k_{cat} and K_m of isopropanol by $LADH^{Co,S48A}$ are not measurable because K_m is much larger than 2 M (Supplementary Fig. 8) and $LADH^{Co,S48A}$ quickly denatured and precipitated out once the isopropanol concentration was above 2 M.

Supplementary Table 9. Michaelis-Menten kinetics of benzaldehyde hydrogenation by LADH and competitive inhibition kinetics of CXF

	Benzaldehyde hydrogenation[a]			CXF inhibition[b]
LADH variants	k_{cat} s^{-1}	K_m μM	k_{cat}/K_m mM^{-1} s^{-1}	K_i μM
Wildtype $LADH^{Zn}$	24.5 ± 0.4	41 ± 2	598 ± 31	5.2 ± 0.2
$LADH^{S48T}$	11.6 ± 0.4	647 ± 57	17.9 ± 1.7	47 ± 1
$LADH^{S48A}$	0.030 ± 0.001	1500 ± 113	0.020 ± 0.002	378 ± 9

[a] The reported errors associated with k_{cat} and K_m represent one standard error of the Michaelis-Menten curve fitting. The errors associated with k_{cat}/K_m are based on the error propagations from k_{cat} and K_m.

[b] The errors associated with K_i represent one standard error of the non-linear fitting of the competitive inhibition kinetics.

Supplementary Table 10. Comparison of the binding constant between acetone, acetaldehyde, benzaldehyde, and CXF. The values are reproduced from Supplementary Tables 8 and 9 for convenience.

	Acetone hydrogenation	acetaldehyde hydrogenation[a]	Benzaldehyde hydrogenation	CXF inhibition
LADH variants	$\boldsymbol{K_{\mathrm{m}}}$ **mM**	$\boldsymbol{K_{\mathrm{m}}}$ **mM**	$\boldsymbol{K_{\mathrm{m}}}$ **μM**	$\boldsymbol{K_{\mathrm{i}}}$ **μM**
Wildtype LADH^{Zn}	52 ± 3	0.40	41 ± 2	5.2 ± 0.2
LADH^{S48T}	317 ± 11	0.53	647 ± 57	47 ± 1
LADH^{S48A}	119 ± 15	100	1500 ± 113	378 ± 9

[a] ref. 26

Supplementary Table 11. Electric fields in the active site of LADH and the free energy barriers of acetone dehydrogenation and isopropanol hydrogenation catalyzed by LADH

LADH variants	Active-site electric field[a] MV/cm	Free energy barrier of acetone hydrogenation[b] kcal/mol	Free energy barrier of isopropanol dehydrogenation[b] kcal/mol
Wildtype LADH^{Zn}	-165.1 ± 0.4	19.43 [19.39, 19.47]	18.33 [18.30, 18.37]
LADH^{Co}	-173.64 ± 0.06	17.89 [17.79, 18.01]	17.78 [17.69, 17.89]
LADH^{Cd}	-163.89 ± 0.09	19.65 [19.60, 19.72]	18.48 [18.40, 18.57]
LADH^{Zn,S48T}	-170.9 ± 0.2	18.35 [18.33, 18.37]	17.38 [17.35, 17.41]
LADH^{Zn,S48A}	-138.91 ± 0.06	22.00 [21.94, 22.08]	22.14 [22.11, 22.16]
LADH^{Co,S48T}	-180.5 ± 0.1	17.11 [17.07, 17.16]	16.74 [16.73, 16.76]
LADH^{Co,S48A}	-150.2 ± 0.4	21.23 [21.15, 21.33]	N/A

[a] The errors associated with electric fields are based on one standard deviation of the IR results (Supplementary Table 6).

[b] The free energy barriers ($\Delta G^{\ddagger}$) are calculated based on transition state theory, $\Delta G^{\ddagger} = -RT\ln[k_{\mathrm{cat}}/(k_{\mathrm{B}}T/h)]$, where R, k_B, and h denote the gas constant, Bolzmann's constant, and Planck constant, respectively, and the temperature $T = 296\ K$. The errors associated with free energy barriers are based on the error propagations from the kinetic results (Supplementary Table 8).

Supplementary Table 12. LADH activity for ethanol dehydrogenation

Enzyme[a]	Optimal free metal concentration (mM)[b]	Activity (s^{-1})[c]
Apo LADH	N/A	0.012 ± 0.001
Wildtype $LADH^{Zn}$	0.3	0.59 ± 0.01
$LADH^{Cd}$	0.035 (1.1 eq to enzyme)	0.15 ± 0.01
$LADH^{Co}$	200	1.25 ± 0.02
$LADH^{Co,S48T}$	200	1.41 ± 0.02

[a] The concentration of the enzyme used for the kinetic measurements is 0.033 mM.

[b] The concentration of the free metal ions used for metal insertion that gave the highest activity (see Fig. 2b).

[c] The activity was calculated based on the total number of apo LADH used for metal insertion. Data are presented as mean values +/- SD based on n=3 independent replicates.

References

1 Zheng, C. *et al.* A two-directional vibrational probe reveals different electric field orientations in solution and an enzyme active site. *Nat. Chem.* **14**, 891-897 (2022).

2 Park, D. H. & Plapp, B. V. Isoenzymes of horse liver alcohol dehydrogenase active on ethanol and steroids. Cdna cloning, expression, and comparison of active sites. *J. Biol. Chem.* **266**, 13296-13302 (1991).

3 Maret, W. *et al.* Site-specific substituted cobalt(II) horse liver alcohol dehydrogenases. Preparation and characterization in solution, crystalline and immobilized state. *Eur. J. Biochem.* **98**, 501-512 (1979).

4 Sytkowski, A. J. & Vallee, B. L. Cd-109 as a probe of the metal-binding sites in horse liver alcohol-dehydrogenase. *Biochemistry* **18**, 4095-4099 (1979).

5 Dhar, S. K. *Metal ions in biological systems : Studies of some biochemical and environmental problems*. 1st 1973. edn, (Plenum Press, 1973).

6 Holmquist, B., Kaden, T. A. & Vallee, B. L. Magnetic circular dichroic spectra of cobalt(ii) substituted metalloenzymes. *Biochemistry* **14**, 1454-1461 (1975).

7 Lindskog, S. & Nyman, P. O. Metal-binding properties of human erythrocyte carbonic anhydrases. *Biochim. Biophys. Acta* **85**, 462-474 (1964).

8 Riordan, J. F. Biochemistry of zinc. *Medical Clinics of North America* **60**, 661-674 (1976).

9 Simpson, R. T. & Vallee, B. L. Two differentiable classes of metal atoms in alkaline phosphatase of eschericha coli. *Biochemistry* **7**, 4343-4350 (1968).

10 Werth, M. T., Tang, S.-F., Formicka, G., Zeppezauer, M. & Johnson, M. K. Magnetic circular dichroism and electron paramagnetic resonance studies of cobalt-substituted horse liver alcohol dehydrogenase. *Inorg. Chem.* **34**, 218-228 (1995).

11 Makinen, M. W. & Yim, M. B. Coordination environment of the active-site metal ion of liver alcohol dehydrogenase. *Proc. Natl. Acad. Sci. U. S. A.* **78**, 6221-6225 (1981).

12 Sekhar, V. C. & Plapp, B. V. Rate constants for a mechanism including intermediates in the interconversion of ternary complexes by horse liver alcohol dehydrogenase. *Biochemistry* **29**, 4289-4295 (1990).

13 Boxer, S. G. Stark realities. *J. Phys. Chem. B* **113**, 2972-2983 (2009).

14 Bublitz, G. U. & Boxer, S. G. Stark spectroscopy: Applications in chemistry, biology, and materials science. *Annu. Rev. Phys. Chem.* **48**, 213-242 (1997).

15 Schneider, S. H., Kozuch, J. & Boxer, S. G. The interplay of electrostatics and chemical positioning in the evolution of antibiotic resistance in TEM beta-lactamases. *ACS Cent. Sci.* **7**, 1996-2008 (2021).

16 Yahashiri, A., Rubach, J. K. & Plapp, B. V. Effects of cavities at the nicotinamide binding site of liver alcohol dehydrogenase on structure, dynamics and catalysis. *Biochemistry* **53**, 881-894 (2014).

17 Wratten, C. C. & Cleland, W. W. Product inhibition studies on yeast and liver alcohol dehydrogenases. *Biochemistry* **2**, 935-941 (1963).

18 Bahnson, B. J., Park, D. H., Kim, K., Plapp, B. V. & Klinman, J. P. Unmasking of hydrogen tunneling in the horse liver alcohol dehydrogenase reaction by site-directed mutagenesis. *Biochemistry* **32**, 5503-5507 (1993).

19 Kim, K. & Plapp, B. V. Substitutions of amino acid residues in the substrate binding site of horse liver alcohol dehydrogenase have small effects on the structures but significantly affect catalysis of hydrogen transfer. *Biochemistry* **59**, 862-879 (2020).
20 Kvassman, J. & Pettersson, G. Kinetic transients in the reduction of aldehydes catalysed by liver alcohol dehydrogenase. *Eur. J. Biochem.* **69**, 279-287 (1976).
21 Luisi, P. L. & Favilla, R. Mechanistic studies on horse liver alcohol dehydrogenase. Influence of the different premixings on the transient kinetics of aldehyde reductions. *Biochemistry* **11**, 2303-2310 (1972).
22 McFarland, J. T. & Bernhard, S. A. Catalytic steps during the single-turnover reduction of aldehydes by alcohol dehydrogenase. *Biochemistry* **11**, 1486-1493 (1972).
23 Adolph, H. W., Kiefer, M. & Zeppezauer, M. in *Enzymology and molecular biology of carbonyl metabolism 4* (eds Henry Weiner, David W. Crabb, & T. Geoffrey Flynn) 401-410 (Springer US, 1993).
24 Adolph, H. W., Maurer, P., Schneider-Bernlohr, H., Sartorius, C. & Zeppezauer, M. Substrate specificity and stereoselectivity of horse liver alcohol dehydrogenase. Kinetic evaluation of binding and activation parameters controlling the catalytic cycles of unbranched, acyclic secondary alcohols and ketones as substrates of the native and active-site-specific Co(II)-substituted enzyme. *Eur. J. Biochem.* **201**, 615-625 (1991).
25 Al-Karadaghi, S. *et al.* Refined crystal structure of liver alcohol dehydrogenase-NADH complex at 1.8 a resolution. *Acta Crystallographica Section D* **50**, 793-807 (1994).
26 Kim, K. & Plapp, B. V. Inversion of substrate stereoselectivity of horse liver alcohol dehydrogenase by substitutions of ser-48 and phe-93. *Chem Biol Interact* **276**, 77-87 (2017).
27 Haldane, J. B. S. *Enzymes*. (MIT Press, 1930).
28 Bonitatibus, P. J. *et al.* Reversible catalytic dehydrogenation of alcohols for energy storage. *Proc. Natl. Acad. Sci. U. S. A.* **112**, 1687-1692 (2015).
29 Fourmond, V., Plumere, N. & Leger, C. Reversible catalysis. *Nat. Rev. Chem.* **5**, 348-360 (2021).
30 Villa, J. & Warshel, A. Energetics and dynamics of enzymatic reactions. *J. Phys. Chem. B* **105**, 7887-7907 (2001).
31 Agarwal, P. K., Webb, S. P. & Hammes-Schiffer, S. Computational studies of the mechanism for proton and hydride transfer in liver alcohol dehydrogenase. *J. Am. Chem. Soc.* **122**, 4803-4812 (2000).
32 Cui, Q., Elstner, M. & Karplus, M. A theoretical analysis of the proton and hydride transfer in liver alcohol dehydrogenase (LADH). *J. Phys. Chem. B* **106**, 2721-2740 (2002).